A parabolic-elliptic-hyperbolic system of Keller-Segel type: numerical analysis and simulation

A. Fernandes, J. A. Ferreira, G. Pena
University of Coimbra, CMUC, Department of Mathematics, Coimbra, Portugal
augusto98@outlook.com, ferreira@mat.uc.pt, goncalo.pena@uc.pt

January 21, 2026

Abstract

This paper aims to study, from a numerical point of view, a system of partial differential equations defined by a parabolic, an elliptic and a hyperbolic equation that can be used to describe cell migration in elastic tissues that integrates *chemotaxis*, interstitial fluid pressure and tissue displacement. The system couples a Keller-Segel type system for cell density and chemical concentration with an elliptic equation for fluid pressure and a wave-type equation for displacement. We propose a semidiscrete nonuniform finite difference method to approximate the continuous system. Furthermore, we derive second-order spatial error estimates for all system variables using a suitable discrete norm. Finally, numerical simulations validate the theoretical results and demonstrate the interplay between *chemotaxis* and tissue mechanics.

Keywords: *Chemotaxis*, tissue displacement, finite difference method, convergence analysis.

1 Introduction

In this paper our aim is to propose a numerical method for the following Keller-Segel (KS) type system

$$\begin{cases} \dfrac{\partial b}{\partial t} + \nabla\cdot\left(\left(\phi(\nabla c, c, \nabla p) + \dfrac{\partial \mathbf{u}}{\partial t}\right) b\right) = \nabla\cdot(D_b(b,c)\nabla b) + f(b,c), & (1)\\ \dfrac{\partial c}{\partial t} + \nabla\cdot\left(\left(\psi(\nabla p) + \dfrac{\partial \mathbf{u}}{\partial t}\right) c\right) = \nabla\cdot(D_c(b,c)\nabla c) + g(b,c), & (2)\\ -\nabla\cdot\left(D_p(p)\nabla p - \dfrac{\partial \mathbf{u}}{\partial t}\right) = q(p), & (3)\\ \rho\dfrac{\partial^2 \mathbf{u}}{\partial t^2} = \boldsymbol{\nabla}\cdot\left(\dfrac{E_0}{2}\left(\boldsymbol{\nabla}\mathbf{u} + \boldsymbol{\nabla}\mathbf{u}^T\right)\right) - \nabla p, & (4) \end{cases}$$

where $\Omega = (0,1)^2$, $t \in (0,T]$ and b, c, p and $\mathbf{u}$[1] represent, respectively, cell density, chemical signal concentration, interstitial fluid pressure and tissue displacement. The boundary of Ω, $\partial\Omega$, is decomposed

[1]We use bold letters to denote vector or matrix valued functions. We also use the notation $\boldsymbol{\nabla}\mathbf{u}$ for the Jacobian matrix of $\mathbf{u}$ and the divergence term $(\boldsymbol{\nabla}\cdot)$ is interpreted per row.

as $\partial\Omega = \Gamma_1 \cup \Gamma_2$, with $\Gamma_1 \cap \Gamma_2 = \emptyset$ and this system is complemented with initial conditions

$$\begin{cases} b(x,y,0) = b_0(x,y), \quad (x,y) \in \Omega, & (5)\\ c(x,y,0) = c_0(x,y), \quad (x,y) \in \Omega, & (6)\\ \dfrac{\partial \mathbf{u}}{\partial t}(x,y,0) = \mathbf{h}_1(x,y), \quad (x,y) \in \Omega, & (7)\\ \mathbf{u}(x,y,0) = \mathbf{h}_2(x,y), \quad (x,y) \in \Omega, & (8) \end{cases}$$

where b_0, c_0 and $\mathbf{h}_1, \mathbf{h}_2$ are known functions. The differential system (1)-(8) is complemented with suitable Dirichlet boundary conditions for all variables. In the differential system (1)-(4), $\mathbf{u} = (u_1, u_2)$, $b, c, p, u_1, u_2 : \overline{\Omega} \times [0,T] \longrightarrow \mathbb{R}$, $q : \mathbb{R} \longrightarrow \mathbb{R}$, $f, g : \mathbb{R}^2 \longrightarrow \mathbb{R}$, D_b, D_c, and D_p are diagonal matrices depending on b and c, $D_{b,ii} : \mathbb{R}^2 \longrightarrow \mathbb{R}$, $i = 1, 2$,

$$D_b(b,c) = \begin{bmatrix} D_{b,11}(b,c) & 0 \\ 0 & D_{b,22}(b,c) \end{bmatrix}, \tag{9}$$

with D_c and D_p being defined analogously, $\phi_i : \mathbb{R}^3 \longrightarrow \mathbb{R}$, $\psi_i : \mathbb{R}^2 \longrightarrow \mathbb{R}$, $i = 1, 2$ and

$$\phi(\nabla c, c, \nabla p) = \begin{bmatrix} \phi_1\left(\frac{\partial c}{\partial x}, c, \frac{\partial p}{\partial x}\right) \\ \phi_2\left(\frac{\partial c}{\partial y}, c, \frac{\partial p}{\partial y}\right) \end{bmatrix}, \tag{10}$$

$$\psi(\nabla p) = \begin{bmatrix} \psi_1\left(\frac{\partial p}{\partial x}\right) \\ \psi_2\left(\frac{\partial p}{\partial y}\right) \end{bmatrix}. \tag{11}$$

A simplified version of the last system has already been studied in the literature. In fact, the following version of the differential system (1)-(4)

$$\begin{cases} \dfrac{\partial b}{\partial t} + \nabla\cdot((\phi(\nabla c, c, \nabla p))b) = \nabla\cdot(D_b(b,c)\nabla b) + f(b,c), & (12)\\ \dfrac{\partial c}{\partial t} + \nabla\cdot((\psi(\nabla p))c) = \nabla\cdot(D_c(b,c)\nabla c) + g(b,c), & (13)\\ -\nabla\cdot(D_p(b,c,p)\nabla p) = q(b,c,p). & (14) \end{cases}$$

was studied in [11] from a numerical point of view. This system can be used to describe cell migration driven by the spatial distribution of a chemoattractant enhanced by the interstitial fluid pressure. In this scenario, $D_j, j = b, c, p$, denotes the cell, chemical signal and pressure diffusivity, respectively. The function $\phi(\nabla c, c, \nabla p)$ represents the cell's sensitivity to interstitial flow and chemical's concentration while $\psi(\nabla p)$ governs the chemical sensitivity to interstitial flow. Moreover, f and g represent cell growth/death and chemoattractant production/degradation rates, respectively, and q is a source term that describes fluid exchanges between the extracellular matrix (ECM) and the capillaries.

Classically, cell migration driven by the concentration of a chemoattractant, is mathematically described by the KS system (see [18, 19] and [1] for a review of several improvements of the classical model). This system has been extensively studied in the literature, both from a theoretical and numerical point of view, see for instance [2, 6, 10, 14, 28] and the references therein. Although the standard KS system effectively describes cell movement in response to chemical concentration gradients, it disregards environmental effects on cells. The importance of considering the interstitial fluid pressure associated with cell migration has been addressed in several studies, see for instance [20, 24–26, 31, 35].

We also mention the reference [29] as a particular experimental study where the effect of interstitial fluid flow on cell migration was documented. Keller-Segel type models incorporating fluid flow were proposed and numerically explored from analytical and/or simulation perspectives. Without being exhaustive we mention [3, 5, 7, 9, 21, 32, 36]. It should be pointed out that significant work has been done for the Keller-Segel-Navier-Stokes system, see for instance [4, 8, 15, 16, 23, 33, 38].

In [11] an IMEX method was proposed that combines a finite difference spatial discretization that can be seen as a fully discrete (in space) piecewise linear finite element discretization with implicit-explicit (IMEX) time integration to treat the nonlinear terms. Sharp second-order superconvergence estimates (in space) with respect to a discrete H^1-norm were deduced by using the Bramble-Hilbert Lemma. This enabled the reduction of the smoothness assumptions usually required if the traditional truncation error analysis is followed. Moreover, the KS-flow system was validated against experimental data from [29] on a chemokine predominantly secreted by lymphatic endothelial cells.

Regarding the mechanical influence of the underlying tissue on cell migration, it has been observed that cells tend to migrate from softer to stiffer regions of the tissue, a phenomenon known as *durotaxis*, see for instance [17, 22, 27]. When (visco)elastic tissues deform due to the (visco)elastic response induced by the fluid flow's pressure, tissue displacement is greater in softer regions and smaller in stiffer regions. Consequently, the tissue's magnitude of the velocity is higher in soft regions when compared with stiff ones, which naturally drives cell migration from soft to stiff regions. In a certain sense, this process may be interpreted as a form of negative *durotaxis* [17]. In pattern formation, cell migration is a consequence of the physical interactions between cells and their local surroundings. The influence of viscoelastic properties in pattern formation is studied in [34] where the authors consider different stress-strain constitutive equations for the ECM. Other mechanochemical models of pattern formation were proposed in the literature, see [34] and its references for a critic analysis of different models.

The differential system (1)-(4) can be considered to describe cell migration driven by a chemoattractant gradient and fluid flow in a poroelastic tissue that deforms under the action of the fluid's pressure. In this context, the two component displacement field $\mathbf{u}$ is linked with the strain tensor by

$$\boldsymbol{\varepsilon}(\mathbf{u}) = \frac{1}{2}(\boldsymbol{\nabla}\mathbf{u} + \boldsymbol{\nabla}\mathbf{u}^T).$$

As in [12, 30], assuming that the relevant forces acting in the poroelastic tissue are the stress, $\boldsymbol{\sigma}$, developed by the internal structure and the interstitial fluid pressure p (assuming that the inertial and gravitational forces are neglected) then the total force $\mathbf{F}$ acting in the porous tissue is given by

$$\mathbf{F} = \boldsymbol{\sigma} - p\mathbf{I}. \tag{15}$$

Assuming that the tissue is an isotropic linear elastic medium, we consider $\boldsymbol{\sigma} = E_0\boldsymbol{\varepsilon}$, where E_0 denotes Young's modulus, and combining Newton's Second Law and (15), we obtain (4).

The objective of this paper is to study a finite difference method (FDM) to approximate the solution of the system of partial differential equations (1) to (4) combining the effects of cell migration with fluid pressure and tissue displacement. Its main contributions are the way the displacement equation (4) is discretized and coupled with the remaining discrete version of the KS system, equations (1) and (2), and the fluid pressure, equation (3), as well as the analysis of the convergence of the method. To our

knowledge, this is the first study where the convergence of a scheme is established for the KS system coupled with the fluid pressure equation and tissue displacement. We highlight that equation (4) has mixed derivatives of the displacement's components, which requires special attention in their discretizations. The coupling also introduces significant analytical challenges, namely, deriving suitable spatial *a priori* error estimates for the approximate displacement field of $\mathbf{u}$ and proving uniform boundedness for the numerical approximations of $\mathbf{u}'$. The latter is crucial to control the error terms arising from the convective terms in equations (1) and (2). The spatial discretization is defined by considering a nonuniform rectangular partition on Ω and our FDM can be seen as a fully discrete piecewise linear finite element approximation defined in the triangulations associated with the rectangular partition. We derive second-order spatial error estimates for all variables of the system under suitable smoothness assumptions. The analysis relies on discrete versions of classical inequalities, such as Poincaré and Sobolev inequalities, adapted to the nonuniform grid setting. Bramble-Hilbert Lemma is the main tool in the construction of the error estimates that lead to sharp estimates in what concerns the smoothness of the continuous solution.

This paper is structured as follows. Section 2 introduces the semidiscrete FDM to approximate the solution of the system of equations (1) to (8) and presents useful preliminary results. Section 3 derives *a priori* error estimates for the proposed FDM under suitable smoothness assumptions. Finally, Section 4 presents numerical simulations to illustrate the theoretical results and an extensive study on the interplay between *chemotaxis* and tissue displacement in the context of cell migration.

2 The semidiscrete approximation

2.1 Discrete operators

Let Λ be a sequence of vectors $H = (\mathbf{h}, \mathbf{k})$, $\mathbf{h} = (h_1, h_2, \ldots, h_N), \mathbf{k} = (k_1, k_2, \ldots, k_M)$, with $h_i, k_j > 0$, $i = 1, \ldots, N$, $j = 1, \ldots, M$, such that $\|\mathbf{h}\|_1 = \|\mathbf{k}\|_1 = 1$ (with $\|\cdot\|_1$ being the standard vector 1-norm) and

$$H_{\max} = \max\left\{ \max_{i=1,\ldots,N} h_i, \max_{j=1,\ldots,M} k_j \right\}.$$

We introduce the nonuniform finite difference grid

$$\overline{\Omega}_H = \{(x_i, y_j) \in \mathbb{R}^2 : x_i = x_{i-1} + h_i,\, y_j = y_{j-1} + k_j, i = 1, \ldots, N, j = 1, \ldots, M\},$$

with $x_0 = y_0 = 0$, $x_N = y_M = 1$.

We set $\Omega_H = \overline{\Omega}_H \cap \Omega$ and $\partial\Omega_H = \overline{\Omega}_H \cap \partial\Omega$. Let V_H denote the set of grid functions defined in $\overline{\Omega}_H$ and let $V_{H,0} \subset V_H$ be the subset of grid functions that are zero on $\partial\Omega_H$. We also define $\mathcal{T}_H$ as the partition of $\overline{\Omega}$ into triangles induced by the grid $\overline{\Omega}_H$. The triangles are obtained from the nonuniform rectangular partition $\overline{\Omega}_H$ by adding a diagonal in each rectangle $[x_{i-1}, x_i] \times [y_{j-1}, y_j]$. If $\Delta \in \mathcal{T}_H$, by $\operatorname{diam}(\Delta)$ we represent the diameter of Δ.

To formulate the numerical scheme, we introduce a few discrete operators. For the difference operators, we explicitly define the components for the x-direction (subscripted with "$_x$"). The corresponding y-direction components are defined in the same way. For the average operators, we also define the component in the x-direction, subscripted with "$_h$" and in the y-direction, subscripted with "$_k$".

The difference operators in the x-direction are

$$\begin{aligned} D_{-x}u_H(x_i,y_j) &= \frac{u_H(x_i,y_j)-u_H(x_{i-1},y_j)}{h_i}, && i=1,\ldots,N,\\ D_{c,x}u_H(x_i,y_j) &= \frac{u_H(x_{i+1},y_j)-u_H(x_{i-1},y_j)}{h_i+h_{i+1}}, && i=1,\ldots,N-1,\\ D_x^*u_H(x_i,y_j) &= \frac{u_H(x_{i+1},y_j)-u_H(x_i,y_j)}{h_{i+1/2}}, && i=0,\ldots,N-1, \end{aligned}$$

where $j=0,\ldots,M$ and $h_{i+1/2}=\frac{1}{2}(h_{i+1}+h_i)$, $i=1,\ldots,N-1$. These are used to build the vector operators that act on V_H functions, $\nabla_H=(D_{-x},D_{-y})$, $\nabla_H^*=(D_x^*,D_y^*)$ and $\nabla_{c,H}=(D_{c,x},D_{c,y})$. We also introduce, for $\mathbf{u}_H=(u_{H,1},u_{H,2})$, the notations $\boldsymbol{\nabla}_H\mathbf{u}_H$ as the matrix whose rows are $(\nabla_H u_{H,i})$, $i=1,2$, and $\boldsymbol{\nabla}_H^*\cdot A_H$ (where A_H is a 2×2 matrix with elements in V_H) as the row-wise application of the discrete divergence operator $(\nabla_H^*\cdot)$.

In the context of discrete difference operators, we introduce the operator D_h as the weighted difference operator

$$D_hu_H(x_i,y_j)=\frac{h_i}{h_i+h_{i+1}}D_{-x}u_H(x_{i+1},y_j)+\frac{h_{i+1}}{h_i+h_{i+1}}D_{-x}u_H(x_i,y_j),$$

for $i=1,\ldots,N-1$ and $j=0,\ldots,M$, with D_k and D_H being defined as in the previous cases. We also introduce the average operator

$$M_hu_H(x_i,y_j)=\frac{u_H(x_i,y_j)+u_H(x_{i-1},y_j)}{2},\ i=1,\ldots,N,\ j=0,\ldots,M, \tag{16}$$

with M_k and M_H defined analogously.

Finally, we introduce the standard restriction operator, $R_H : C(\Omega)\longrightarrow V_H$, as $R_Hf(x_i,y_j)=f(x_i,y_j)$, for all $x_i,y_j\in\overline{\Omega}_H$ and $f\in C(\Omega)$.

2.2 Inner products and norms

We now proceed to introduce several inner products and norms that will be useful in the convergence analysis of the FDM equations (23) to (26).

For scalar grid functions u_H, w_H in V_H, we define the discrete L^2 inner product,

$$(u_H,w_H)_H=\sum_{(x_i,y_j)\in\Omega_H}h_{i+1/2}k_{j+1/2}u_H(x_i,y_j)w_H(x_i,y_j), \tag{17}$$

and denote the its induced norm by $\|\cdot\|_H$. To handle the discrete derivatives, we introduce bilinear forms (which are inner products in $V_{H,0}$),

$$(u_H,w_H)_{x,+}=\sum_{i=1}^{N}\sum_{j=1}^{M-1}h_ik_{j+1/2}u_H(x_i,y_j)w_H(x_i,y_j),$$

and, in a similar way, $(\cdot,\cdot)_{y,+}$. Let $\|\cdot\|_{x,+}$ and $\|\cdot\|_{y,+}$ denote the norms (in $V_{H,0}$ only) induced by these bilinear forms. For $u_H, w_H\in V_H$, we now define

$$(u_H,w_H)_+=(u_H,w_H)_{x,+}+(u_H,w_H)_{y,+}, \tag{18}$$

which allows us to express the norm of the discrete gradient as

$$\begin{aligned}\|\nabla_H u_H\|_+^2 &= \|D_{-x}u_H\|_{x,+}^2 + \|D_{-y}u_H\|_{y,+}^2 \\ &= (D_{-x}u_H, D_{-x}u_H)_{x,+} + (D_{-y}u_H, D_{-y}u_H)_{y,+}.\end{aligned}$$

Consequently, we can define the discrete H^1-norm,

$$\|u_H\|_{1,H} = \left(\|u_H\|_H^2 + \|\nabla_H u_H\|_+^2\right)^{1/2}, \quad u_H \in V_H. \tag{19}$$

Finally, we introduce in V_H the discrete L^∞-norm,

$$\|u_H\|_{H,\infty} = \max_{(x_i,y_j)\in\overline{\Omega}_H} |u_H(x_i, y_j)|, \tag{20}$$

for all $u_H \in V_H$, with the obvious extension to vector grid functions.

Remark 1. To simplify the presentation, we will often omit constants in inequalities that do not depend on the discretization parameter H and time. That means that if C denotes a positive constant, independent of H and t, such that $A \leq CB$, holds, we will simply write $A \lesssim B$.

2.3 Extension to vector grid functions

The previous definitions extend to vector grid functions $\mathbf{u}_H = (u_{H,1}, u_{H,2})$, $\mathbf{w}_H = (w_{H,1}, w_{H,2}) \in [V_H]^2$ naturally. The corresponding inner products are

$$\begin{aligned}(\mathbf{u}_H, \mathbf{w}_H)_H &= (u_{H,1}, w_{H,1})_H + (u_{H,2}, w_{H,2})_H, \\ (\mathbf{u}_H, \mathbf{w}_H)_+ &= (u_{H,1}, w_{H,1})_{x,+} + (u_{H,2}, w_{H,2})_{y,+},\end{aligned}$$

and the associated norms are denoted by $\|\mathbf{u}_H\|_H$ and $\|\mathbf{u}_H\|_+$, respectively. For the discrete operators ∇_H, D_H or M_H, we can define how they are applied to a vector function $\mathbf{u}_H$ through componentwise operations. For example, in the case of ∇_H, we have

$$\nabla_H \mathbf{u}_H = (D_{-x}u_{H,1}, D_{-y}u_{H,2}).$$

2.4 Useful inequalities and identities

For the grid spaces, inner products and norms introduced in Sections 2.1 to 2.3 we recall some useful results. The proof of the following propositions is a straightforward applications of summation by parts and is therefore omitted.

Proposition 1 (Discrete Poincaré inequality)**.** *For all $v_H \in V_{H,0}$, it holds that*

$$\|v_H\|_H \leq \|\nabla_H v_H\|_+.$$

Proposition 2. *For all $v_H \in V_H$ and $w_H \in V_{H,0}$, we have*

$$(\nabla_H^* \cdot v_H, w_H)_H = -(v_H, \nabla_H w_H)_+.$$

Proposition 3. *Let $\mathbf{u}_H \in [V_{H,0}]^2$ and $v_H \in V_{H,0}$. We have*

$$(\nabla_{c,H}\cdot \mathbf{u}_H, v_H)_H = -(M_H \mathbf{u}_H, \nabla_H v_H)_+.$$

Proposition 4. *For $v_H, w_H \in V_{H,0}$, the following identities hold*

$$(D_{c,x}v_H, w_H)_H = -(v_H, D_{c,x}w_H)_H,$$
$$(D_{c,y}v_H, w_H)_H = -(v_H, D_{c,y}w_H)_H.$$

Proposition 5. *For $v_H \in V_H$, it holds that*

$$\|D_{c,x}v_H\|_H \leq \|D_{-x}v_H\|_{x,+},$$
$$\|D_{c,y}v_H\|_H \leq \|D_{-y}v_H\|_{y,+}.$$

2.5 Function spaces

We introduce the Sobolev spaces, $W^{s,p}(\Omega)$, for functions defined in the spatial domain Ω using standard notation. The norm associated with this space is $\|\cdot\|_{W^{s,p}(\Omega)}$, for $1 \leq p \leq \infty$ and $s \geq 0$. In the case $p = 2$, we denote $H^s(\Omega) = W^{s,2}(\Omega)$, with norm $\|\cdot\|_{H^s(\Omega)}$ and in the case $s = 0$, we use $L^p(\Omega) = W^{0,p}(\Omega)$, with norm $\|\cdot\|_{L^p(\Omega)}$.

For time-dependent problems on the space-time domain $\Omega \times (0, T)$, let X denote a Banach space with norm $\|\cdot\|_X$. We introduce the Bochner spaces, $H^i(0, T; X)$, $i \geq 0$, of the functions with weak derivatives up to order i in time with values in X. This space is imbued with its standard norm, $\|\cdot\|_{H^i(0,T;X)}$. We use the notation $C^m([0, T]; X)$ to denote the space of functions $v : [0, T] \longrightarrow X$ such that $v^{(i)} : [0, T] \longrightarrow X$, $i = 0, \ldots, m$, are continuous. This space is equipped with the norm

$$\|v\|_{C^m([0,T];X)} = \max_{i=0,\ldots,m} \max_{t\in[0,T]} \|v^{(i)}(t)\|_X.$$

For time-valued grid functions $v_H : \overline{\Omega}_H \times [0, T] \longrightarrow \mathbb{R}$, for each $t \in [0, T]$, we denote by $v_H(t) : \overline{\Omega}_H \longrightarrow \mathbb{R}$, the grid function defined by $v_H(t)(x_i, y_j) = v_H(x_i, y_j, t)$, $i = 0, \ldots, N$ and $j = 0, \ldots, M$. Its time derivative is denoted by $v'_H(t)$. These definitions extend in a straightforward way to the vector case.

2.6 Semidiscrete numerical scheme

Before introducing the numerical scheme, we need to define notations to discretize the diffusion and convection terms as well as the source terms. The diffusion and convection terms in equations (1) to (3) involve the operators $D_\alpha(t)$, $\alpha = b, c, p$. If $b_H(t), c_H(t), p_H(t)$ are approximations of $b(t), c(t), p(t)$, respectively, then we define

$$D_{b,H}(t) = \begin{bmatrix} D_{b,11}(M_h b_H(t), M_h c_H(t)) & 0 \\ 0 & D_{b,22}(M_k b_H(t), M_k c_H(t)) \end{bmatrix}, \tag{21}$$

with $D_{c,H}(t)$ and $D_{p,H}(t)$ being defined similarly. The discrete convection-diffusion functions are discretized using the D_h, D_k operators as follows

$$\phi_H(t) = \begin{bmatrix} \phi_1(D_h c_H(t), c_H(t), D_h p_H(t)) \\ \phi_2(D_k c_H(t), c_H(t), D_k p_H(t)) \end{bmatrix}, \quad \psi_H(t) = \begin{bmatrix} \psi_1(D_h p_H(t)) \\ \psi_2(D_k p_H(t)) \end{bmatrix}. \tag{22}$$

Finally, the source terms, $f_H(t), g_H(t)$ and $q_H(t)$ are discretized by evaluation on the grid functions, i.e., taking f_H as an example, $f_H(t) = f(b_H(t), c_H(t))$.

Using these notations, the proposed semidiscrete finite difference method for equations (1) to (8) reads as follows:

find $b_H(t), c_H(t), u_H(t) \in V_{H,0}$ and $p_H(t) \in V_H$ such that $p_H(t) = R_H p_1(t)$ in $\Gamma_{1,H} = \partial\Omega_H \cap \Gamma_1$, $p_H(t) = R_H p_2(t)$ in $\Gamma_{2,H} = \partial\Omega_H \cap \Gamma_2$,

$$\begin{cases} q_H(t) = -\nabla_H^* \cdot (D_{p,H}(t) \nabla_H p_H(t)) + \nabla_{c,H} \cdot \mathbf{u}_H'(t), & (23) \\ \mathbf{u}_H''(t) = \boldsymbol{\nabla}_H^* \cdot \left(\dfrac{E_0}{2} \big(\boldsymbol{\nabla}_H \mathbf{u}_H(t) + (\boldsymbol{\nabla}_H \mathbf{u}_H(t))^T \big) \right) - D_H p_H(t), & (24) \end{cases}$$

and

$$\begin{cases} b_H'(t) + \nabla_{c,H} \cdot \big(\big(\phi_H(t) + \mathbf{u}_H'(t) \big) b_H(t) \big) = \nabla_H^* \cdot (D_{b,H}(t) \nabla_H b_H(t)) + f_H(t), & (25) \\ c_H'(t) + \nabla_{c,H} \cdot \big(\big(\psi_H(t) + \mathbf{u}_H'(t) \big) c_H(t) \big) = \nabla_H^* \cdot (D_{c,H}(t) \nabla_H c_H(t)) + g_H(t), & (26) \end{cases}$$

in $\Omega_H \times (0, T]$ and $\mathbf{u}_H = (u_{H,1}, u_{H,2})$. The system of equations (23) to (26) is complemented with the initial conditions

$$\begin{cases} b_H(0) = R_H b_0, \\ c_H(0) = R_H c_0, \end{cases} \tag{27}$$

and

$$\begin{cases} \mathbf{u}_H'(0) = R_H \mathbf{h}_1, \\ \mathbf{u}_H(0) = R_H \mathbf{h}_2, \end{cases} \tag{28}$$

in Ω_H.

Using Propositions 2 and 4, we rewrite equations (23) to (26) in a form suitable for the upcoming convergence analysis, that is, find $b_H(t), c_H(t), u_{H,1}(t), u_{H,2}(t) \in V_{H,0}$, $p_H(t) \in V_H$, such that $p_H(t) = R_H p_1$ in $\Gamma_{1,H}$, $p_H(t) = R_H p_2$ in $\Gamma_{2,H}$, and

$$(D_{p,H}(t) \nabla_H p_H(t), \nabla_H w_{p,H})_+ - (M_H \mathbf{u}_H'(t), \nabla_H w_{p,H})_+ = (q_H(t), w_{p,H})_H, \tag{29}$$

$$\begin{aligned} (u_{H,1}''(t), w_{H,1})_H = &-\frac{E_0}{2} (D_{c,y} u_{H,2}(t), D_{c,x} w_{H,1})_H - E_0 (D_{-x} u_{H,1}(t), D_{-x} w_{H,1})_{x,+} \\ &- \frac{E_0}{2} (D_{-y} u_{H,1}(t), D_{-y} w_{H,1})_{y,+} - (D_h p_H(t), w_{H,1})_H, \end{aligned} \tag{30}$$

$$\begin{aligned} (u_{H,2}''(t), w_{H,2})_H = &-\frac{E_0}{2} (D_{c,x} u_{H,1}(t), D_{c,y} w_{H,2})_H - E_0 (D_{-y} u_{H,2}(t), D_{-y} w_{H,2})_{y,+} \\ &- \frac{E_0}{2} (D_{-x} u_{H,2}(t), D_{-x} w_{H,2})_{x,+} - (D_k p_H(t), w_{H,2})_H, \end{aligned} \tag{31}$$

$$\begin{aligned} (b_H'(t), w_{b,H})_H = &(M_H \big(\big(\phi_H(t) + \mathbf{u}_H'(t) \big) b_H(t) \big) - D_{b,H}(t) \nabla_H b_H(t), \nabla_H w_{b,H})_+ \\ &+ (f_H(t), w_{b,H})_H, \end{aligned} \tag{32}$$

$$\begin{aligned} (c_H'(t), w_{c,H})_H = &(M_H \big(\big(\psi_H(t) + \mathbf{u}_H'(t) \big) c_H(t) \big) - D_{c,H}(t) \nabla_H c_H(t), \nabla_H w_{c,H})_+ \\ &+ (g_H(t), w_{c,H})_H, \end{aligned} \tag{33}$$

for all $w_{p,H}, w_{H,1}, w_{H,2}, w_{b,H}, w_{c,H} \in V_{H,0}$. The system of equations (29) to (33) is defined for $t \in (0, T]$ and it is complemented with the initial conditions

$$\begin{cases} (\mathbf{u}_H'(0), \mathbf{v}_1)_H = (R_H \mathbf{h}_1, \mathbf{v}_1)_H, \\ (\mathbf{u}_H(0), \mathbf{v}_2)_H = (R_H \mathbf{h}_2, \mathbf{v}_2)_H, \end{cases}$$

for all $\mathbf{v}_1, \mathbf{v}_2 \in [V_{H,0}]^2$ and

$$\begin{cases} (b_H(0), w_1)_H = (R_H b_0, w_1)_H, \\ (c_H(0), w_2)_H = (R_H c_0, w_2)_H, \end{cases}$$

for all $w_1, w_2 \in V_{H,0}$.

We remark that this form of the semidiscrete FDM system is akin to a Galerkin method with numerical integration.

2.7 Assumptions

We make the following assumptions on the nonuniform finite difference grid $\overline{\Omega}_H$ and the coefficient and source functions of the system of equations (1) to (8).

(**I**) Let $\{\overline{\Omega}_H\}_{H\in\Lambda}$ denote a sequence of grids. The grids are said to be *quasi-uniform* if there exists a constant $C_{qu} > 0$ such that for all $H \in \Lambda$,

$$\frac{H_{\max}}{H_{\min}} \leq C_{qu}.$$

(**II**) The diffusion coefficient functions $D_{b,ii} \in W^{2,\infty}(\mathbb{R}^2)$, $i = 1, 2$, are Lipschitz functions, with Lipschitz constant L_{D_b}. Moreover, there exists $D_{b,0} > 0$ such that $D_{b,0} \leq D_{b,ii}$. We impose the same conditions for the similar functions related with D_c and D_p.

(**III**) The functions $\phi_i \in L^\infty(\mathbb{R}^3)$, $i = 1, 2$, are Lipschitz functions with Lipschitz constant L_ϕ. Moreover, there exists C_ϕ such that $|\phi_i| \leq C_\phi$, and $\phi_i(\nabla c(t), c(t), \nabla p(t))b(t) \in H^2(\Omega)$, $i = 1, 2$. (we consider similar assumptions for ψ).

(**IV**) The source terms f, g, q are Lipschitz functions. For $w = f, g, p$, the Lipschitz constant of w is L_w and $w(b(t), c(t)) \in H^2(\Omega)$.

Remark 2. In the upcoming analysis, the assumption (**I**), the quasi-uniformity of the grids, can be avoided if functions ϕ and ψ are independent of ∇c and/or ∇p.

3 Convergence analysis

We establish an error estimate for the spatial errors of the semidiscrete approximations defined by equations (23) to (28). In order to do this, we first present an estimate for the spatial error of the pressure fluid, $E_{p,H}(t)$. Then we present estimates for the spatial error of the semidiscrete approximation for the displacement. Then we combine the estimates obtained and present a bound for $\|\mathbf{u}'_H(t)\|_{H,\infty}$. Finally, we establish error estimates for the semidiscrete approximations of the density of cells and the chemical signal, b and c, respectively.

3.1 Pressure and displacement error estimates

Let $\mathbf{u} = (u_1, u_2)$, $E_{u_j,H}(t) = R_H u_j(t) - u_{H,j}(t)$, $j = 1, 2$, and $E_{\mathbf{u},H}(t) = (E_{u_1,H}(t), E_{u_2,H}(t))$ denote the spatial error of the semidiscrete approximations for the displacement.

Proposition 6 (Estimate for the pressure error)**.** *If the assumptions of Section 2.7 hold,* $p \in H^1(0,T;H^3(\Omega))$, $q(p) \in H^1(0,T;H^2(\Omega))$, $\mathbf{u}' \in H^1(0,T;[H^2(\Omega)]^2)$ *and*

$$L_{D_p}\|p\|_{H^1(0,T;H^3(\Omega))} + L_q < D_{p,0}, \tag{34}$$

then

$$\|\nabla_H E_{p,H}(t)\|_+^2 \lesssim \|E'_{\mathbf{u},H}(t)\|_H^2 + T_{p,H}(t), \tag{35}$$

for $t \in [0,T]$*, where*

$$T_{p,H}(t) = \sum_{\Delta\in\mathcal{T}_H} (\operatorname{diam}(\Delta))^4 \Big(\|p(t)\|_{H^3(\Delta)}^2 + \|q(p(t))\|_{H^2(\Delta)}^2 + \|\mathbf{u}'(t)\|_{[H^2(\Delta)]^2}^2 \Big). \tag{36}$$

Proof. The proof follows [11, Proposition 4]. □

Remark 3. We highlight that the bound given by inequality (35) directly implies a similar one replacing $\|\nabla_H E_{p,H}(t)\|_+$ by $\|E_{p,H}(t)\|_H$ using the discrete Poincaré inequality given by Proposition 1.

We now turn our attention to estimate the error for the displacement. In this context, we introduce the following notations:

$$D_{x,y}\mathbf{u}(t) = \left(\frac{\partial^2 u_2}{\partial x\,\partial y}, \frac{\partial^2 u_1}{\partial y\,\partial x}\right), \qquad D_{2,x,y}\mathbf{u}(t) = \left(\frac{\partial^2 u_1}{\partial x^2}, \frac{\partial^2 u_2}{\partial y^2}\right),$$
$$D_{2,y,x}\mathbf{u}(t) = \left(\frac{\partial^2 u_1}{\partial y^2}, \frac{\partial^2 u_2}{\partial x^2}\right),$$

$$\mathbb{E}_{\mathbf{u},H}(t) = \|E'_{\mathbf{u},H}(t)\|_H^2 + E_0\|\nabla_H E_{\mathbf{u},H}(t)\|_+^2 + \frac{E_0}{2}\big(\|D_{-y}E_{u_1,H}(t)\|_{y,+}^2 + \|D_{-x}E_{u_2,H}(t)\|_{x,+}^2\big),$$

for $t \in [0,T]$.

Proposition 7 (Estimate for the displacement error)**.** *If* $\mathbf{u} \in [H^2(0,T;H^2(\Omega)) \cap L^2(0,T;H^3(\Omega) \cap H_0^1(\Omega))]^2$, $p \in H^1(0,T;H^3(\Omega))$ *and assuming that the sequence of grids* $\overline{\Omega}_H$ *is quasi-uniform, then, for all* $\varepsilon_p, \varepsilon_Q \neq 0$*, there exists a constant* $C > 0$*, independent of* H *and* t *but dependent on* $\varepsilon_p, \varepsilon_Q$*, such that the following inequality holds:*

$$\begin{aligned}\frac{1}{2}\frac{\mathrm{d}\mathbb{E}_{\mathbf{u},H}}{\mathrm{d}t}(t) \leq &-\frac{E_0}{2}\frac{\mathrm{d}}{\mathrm{d}t}(D_{c,x}E_{u_1,H}(t), D_{c,y}E_{u_2,H}(t))_H + \varepsilon_Q^2\|\nabla_H E_{\mathbf{u},H}(t)\|_+^2 + \\ &+ \varepsilon_p^2\|\nabla_H E_{p,H}(t)\|_+^2 + \frac{2(1+C_{qu})}{\varepsilon_p^2}\|E'_{\mathbf{u},H}(t)\|_H^2 + \frac{dG_H}{dt}(t) + Q_H(t),\end{aligned} \tag{37}$$

for $t \in [0,T]$*, where*

$$\begin{aligned}G_H(t) = &(R_H\mathbf{u}''(t) - (\mathbf{u}''(t))_H, E_{\mathbf{u},H}(t))_H \\ &+ E_0((D_{2,x,y}\mathbf{u}(t))_H, E_{\mathbf{u},H}(t))_H + E_0(\nabla_H R_H\mathbf{u}(t), \nabla_H E_{\mathbf{u},H}(t))_+ \\ &+ \frac{E_0}{2}((D_{2,y,x}\mathbf{u}(t))_H, E_{\mathbf{u},H}(t))_H + \frac{E_0}{2}(\nabla_H R_H\mathbf{u}(t), \nabla_H E_{\mathbf{u},H}(t))_+ \\ &+ \frac{E_0}{2}((D_{x,y}\mathbf{u}(t))_H, E_{\mathbf{u},H}(t))_H + \frac{E_0}{2}(\nabla_{c,H} R_H\mathbf{u}(t), \nabla_{c,H} E_{\mathbf{u},H}(t))_+ \\ &+ (D_H R_H p(t), E_{\mathbf{u},H}(t))_H - ((\nabla p)_H, E_{\mathbf{u},H}(t))_H\end{aligned}$$

and

$$Q_H(t) = C\sum_{\Delta\in\mathcal{T}_H} \operatorname{diam}^4(\Delta)\Big(\|\mathbf{u}'''(t)\|_{[H^2(\Delta)]^2}^2 + \|\mathbf{u}'(t)\|_{[H^3(\Delta)]^2}^2 + \|p'(t)\|_{H^3(\Delta)}^2\Big). \tag{38}$$

Proof. Taking $w_{H,1} = E'_{u_1,H}(t)$ in equation (30) we have

$$\begin{aligned}(u''_{H,1}(t), E'_{u_1,H}(t))_H = &-E_0(D_{-x}u_{H,1}(t), D_{-x}E'_{u_1,H}(t))_{x,+}\\ &-\frac{E_0}{2}(D_{-y}u_{H,1}(t), D_{-y}E'_{u_1,H}(t))_{y,+}\\ &-\frac{E_0}{2}(D_{c,y}u_{H,2}(t), D_{c,x}E'_{u_1,H}(t))_H\\ &-(D_h p_H(t), E'_{u_1,H}(t))_H.\end{aligned} \tag{39}$$

On the other hand, from equation (4) we deduce

$$\begin{aligned}(R_H u''_1(t), E'_{u_1,H}(t))_H = &-E_0(D_{-x}R_H u_1(t), D_{-x}E'_{u_1,H}(t))_{x,+}\\ &-\frac{E_0}{2}(D_{-y}R_H u_1(t), D_{-y}E'_{u_1,H}(t))_{y,+}\\ &-\frac{E_0}{2}(D_{c,y}R_H u_2(t), D_{c,x}E'_{u_1,H}(t))_H\\ &-(D_h R_H p(t), E'_{u_1,H}(t))_H + S_{1,H}(t)\end{aligned} \tag{40}$$

with

$$\begin{aligned}S_{H,1}(t) = &(R_H u''_1(t) - (u''_1(t))_H, E'_{u_1,H}(t))_H\\ &+E_0\left(\left(\frac{\partial^2 u_1}{\partial x^2}(t)\right)_H, E'_{u_1,H}(t)\right)_H + E_0(D_{-x}R_H u_1(t), D_{-x}E'_{u_1,H}(t))_{x,+}\\ &+\frac{E_0}{2}\left(\left(\frac{\partial^2 u_1}{\partial y^2}(t)\right)_H, E'_{u_1,H}(t)\right)_H + \frac{E_0}{2}(D_{-y}R_H u_1(t), D_{-y}E'_{u_1,H}(t))_{y,+}\\ &+\frac{E_0}{2}\left(\left(\frac{\partial^2 u_2}{\partial x\,\partial y}(t)\right)_H, E'_{u_1,H}(t)\right)_H + \frac{E_0}{2}(D_{c,y}R_H u_2(t), D_{c,x}E'_{u_1,H}(t))_H\\ &-\left(\left(\frac{\partial p}{\partial x}(t)\right)_H, E'_{u_1,H}(t)\right)_H + (D_h R_H p(t), E'_{u_1,H}(t))_H.\end{aligned}$$

In the definition of $S_{H,1}(t)$ the following notation was used: if $v \in L^1(\Omega)$, then $(v)_H : \Omega_H \longrightarrow \mathbb{R}$ is given by

$$(v)_H(x_i, y_j) = \frac{1}{|\square_{ij}|}\int_{\square_{ij}} v(x,y)\,\mathrm{d}x\,\mathrm{d}y,$$

for all $(x_i, y_j) \in \Omega_H$. Here, $\square_{ij} = [x_{i-1/2}, x_{i+1/2}] \times [y_{j-1/2}, y_{j+1/2}]$, $x_{i-1/2} = x_{i-1} + \frac{h_i}{2}$, with $x_{i+1/2}$ and $y_{j\pm 1/2}$ being defined analogously.

We observe that $S_{H,1}(t)$ can be represented as

$$S_{H,1}(t) = \frac{\mathrm{d}G_{H,1}}{\mathrm{d}t}(t) + Q_{H,1}(t), \tag{41}$$

with

$$\begin{aligned}G_{H,1}(t) = &(R_H u''_1(t) - (u''_1(t))_H, E_{u_1,H}(t))_H\\ &+E_0\left(\left(\frac{\partial^2 u_1}{\partial x^2}(t)\right)_H, E_{u_1,H}(t)\right)_H + E_0(D_{-x}R_H u_1(t), D_{-x}E_{u_1,H}(t))_{x,+}\\ &+\frac{E_0}{2}\left(\left(\frac{\partial^2 u_1}{\partial y^2}(t)\right)_H, E_{u_1,H}(t)\right)_H + \frac{E_0}{2}(D_{-y}R_H u_1(t), D_{-y}E_{u_1,H}(t))_{y,+}\\ &+\frac{E_0}{2}\left(\left(\frac{\partial^2 u_2}{\partial x\,\partial y}(t)\right)_H, E_{u_1,H}(t)\right)_H + \frac{E_0}{2}(D_{c,y}R_H u_2(t), D_{c,x}E_{u_1,H}(t))_H\\ &-\left(\left(\frac{\partial p}{\partial x}(t)\right)_H, E_{u_1,H}(t)\right)_H + (D_h R_H p(t), E_{u_1,H}(t))_H\end{aligned}$$

and

$$
\begin{aligned}
Q_{H,1}(t) = (R_H u_1'''(t) - (u_1'''(t))_H, E_{u_1,H}(t))_H \\
&+ E_0\bigg(\bigg(\frac{\partial^2 u_1'}{\partial x^2}(t)\bigg)_H, E_{u_1,H}(t)\bigg)_H + E_0(D_{-x}R_H u_1'(t), D_{-x}E_{u_1,H}(t))_{x,+} \\
&+ \frac{E_0}{2}\bigg(\bigg(\frac{\partial^2 u_1'}{\partial y^2}(t)\bigg), E_{u_1,H}(t)\bigg)_H + \frac{E_0}{2}(D_{-y}R_H u_1'(t), D_{-y}E_{u_1,H}(t))_{y,+} \\
&+ \frac{E_0}{2}\bigg(\bigg(\frac{\partial^2 u_2'}{\partial x\,\partial y}(t)\bigg)_H, E_{u_1,H}(t)\bigg)_H + \frac{E_0}{2}(D_{c,y}R_H u_2'(t), D_{c,x}E_{u_1,H}(t))_H \\
&- \bigg(\bigg(\frac{\partial p'}{\partial x}(t)\bigg)_H, E_{u_1,H}(t)\bigg)_H + (D_h R_H p'(t), E_{u_1,H}(t))_H.
\end{aligned}
$$

Combining equations (39) to (41) we derive

$$
\frac{1}{2}\frac{\mathrm{d}\mathbb{E}_{H,1}}{\mathrm{d}t}(t) \le -\frac{E_0}{2}\big(D_{c,y}E_{u_2,H}(t), D_{c,x}E'_{u_1,H}(t)\big)_H - \big(D_h E_{p,H}(t), E'_{u_1,H}(t)\big)_H + \frac{\mathrm{d}G_{H,1}}{\mathrm{d}t}(t) + Q_{H,1}(t),
$$

where $\mathbb{E}_{H,1}(t) = \|E'_{u_1,H}(t)\|_H^2 + E_0\|D_{-x}E_{u_1,H}(t)\|_{x,+}^2 + \frac{E_0}{2}\|D_{-y}E_{u_1,H}(t)\|_{y,+}^2$.

We can perform a similar analysis for the second equation for the displacement and derive an upper bound for $\frac{1}{2}\frac{\mathrm{d}\mathbb{E}_{H,2}}{\mathrm{d}t}(t)$, where

$$
\mathbb{E}_{H,2}(t) = \|E'_{u_2,H}(t)\|_H^2 + E_0\|D_{-y}E_{u_2,H}(t)\|_{y,+}^2 + \frac{E_0}{2}\|D_{-x}E_{u_2,H}(t)\|_{x,+}^2.
$$

Combining both upper bounds, we obtain

$$
\begin{aligned}
\frac{1}{2}\frac{\mathrm{d}\mathbb{E}_{\mathbf{u},H}}{\mathrm{d}t} \le -\frac{E_0}{2}\big((D_{c,x}E_{u_1,H}(t), D_{c,y}E'_{u_2,H}(t))_H + (D_{c,y}E_{u_2,H}(t), D_{c,x}E'_{u_1,H}(t))_H\big) \\
- (D_H E_{p,H}(t), E'_{\mathbf{u},H}(t))_H + \sum_{j=1,2}\bigg(\frac{\mathrm{d}G_{H,j}}{\mathrm{d}t}(t) + Q_{H,j}(t)\bigg),
\end{aligned}
$$

where $G_{H,2}(t)$ and $Q_{H,2}(t)$ are defined as $G_{H,1}(t)$ and $Q_{H,1}(t)$ with convenient modifications.

For the remaining terms, we observe that, for all $\varepsilon_p \neq 0$, we have

$$
\begin{aligned}
\big|(D_H E_{p,H}(t), E'_{\mathbf{u},H}(t))_H\big| &\le 2\sqrt{2}\sqrt{1+C_{qu}}\|\nabla_H E_{p,H}(t)\|_+\|E'_{\mathbf{u},H}(t)\|_H \\
&\le \varepsilon_p^2\|\nabla_H E_{p,H}(t)\|_+^2 + \frac{2(1+C_{qu})}{\varepsilon_p^2}\|E'_{\mathbf{u},H}(t)\|_H^2,
\end{aligned}
$$

and

$$
\frac{\mathrm{d}}{\mathrm{d}t}(D_{c,x}E_{u_1,H}(t), D_{c,y}E_{u_2,H}(t))_H = (D_{c,x}E_{u_1,H}(t), D_{c,y}E'_{u_2,H}(t))_H + (D_{c,y}E_{u_2,H}(t), D_{c,x}E'_{u_1,H}(t))_H.
$$

Finally, using a similar technique as in [13], it can be shown that, for all $\varepsilon_Q \neq 0$, there exists a positive constant C_1, independent of H and t (but dependent on ε_Q), such that

$$
\begin{aligned}
|Q_{H,1}(t)| \le C_1 \sum_{\Delta\in\mathcal{T}_H} \mathrm{diam}^4(\Delta)\Big(\|u_1'''(t)\|_{H^2(\Delta)}^2 + \|u_1'(t)\|_{H^3(\Delta)}^2 + \|u_2'(t)\|_{H^3(\Delta)}^2 + \|p'(t)\|_{H^3(\Delta)}^2\Big) \\
+ \frac{\varepsilon_Q^2}{2}\|\nabla_H E_{u_1,H}(t)\|_{x,+}^2.
\end{aligned}
$$

Since a similar estimate holds for $Q_{H,2}(t)$, combining the previous inequalities and identities concludes the proof. □

Theorem 1. *Let* $\mathbf{u} \in [H^3(0,T;H^2(\Omega)) \cap H^1(0,T;H^3(\Omega)) \cap L^2(0,T;H^3(\Omega) \cap H_0^1(\Omega))]^2$, $p \in H^1(0,T;H^3(\Omega))$, $\mathbf{u}''(0) \in [H^2(\Omega)]^2$, $\mathbf{u}(0) \in [H^3(\Omega)]^2$ *and* $p(0) \in H^3(\Omega)$, *where* $\mathbf{u}$ *and* p *are the solutions of equations* (3) *and* (4). *If the assumptions of Section 2.7 and inequality (34) are satisfied then*

$$\|E'_{\mathbf{u},H}(t)\|_H^2 + \sum_{s=\mathbf{u},p} \|\nabla_H E_{s,H}(t)\|_+^2 \lesssim \|E'_{\mathbf{u},H}(0)\|_H^2 + \|\nabla_H E_{\mathbf{u},H}(0)\|_+^2 + T_{\mathbf{u}}(t), \tag{42}$$

for $t \in [0,T]$, *where*

$$\begin{aligned} |T_{\mathbf{u}}(t)| \lesssim \sum_{\Delta \in \mathcal{T}_H} \operatorname{diam}^4(\Delta) \Big(&\|\mathbf{u}\|^2_{[H^3(0,T;H^2(\Delta))]^2} + \|\mathbf{u}\|^2_{[H^1(0,T;H^3(\Delta))]^2} + \|p\|^2_{H^1(0,T;H^3(\Delta))} \\ &+ \|q(p)\|^2_{L^2(0,T;H^2(\Delta))} + \|\mathbf{u}''(0)\|^2_{[H^2(\Delta)]^2} + \|\mathbf{u}(0)\|^2_{[H^3(\Delta)]^2} + \|p(0)\|^2_{H^3(\Delta)} \Big). \end{aligned}$$

Proof. From the regularity assumptions on $\mathbf{u}$ and p and inequality (34), we can apply Proposition 6 to estimate $\|\nabla_H E_{p,H}(t)\|_+^2$ in inequality (37), obtaining

$$\begin{aligned} \|E'_{\mathbf{u},H}(t)\|_H^2 + E_0 \|\nabla_H E_{\mathbf{u},H}(t)\|_+^2 \leq 2C_1 &\int_0^t \big(\|\nabla_H E_{\mathbf{u},H}(s)\|_+^2 + \|E'_{\mathbf{u},H}(s)\|_H^2 \big) \, \mathrm{d}s \\ &- E_0 (D_{c,x} E_{u_1,H}(t), D_{c,y} E_{u_2,H}(t))_H + S_{u,H}(t), \end{aligned} \tag{43}$$

for $t \in [0,T]$, where

$$\begin{aligned} S_{u,H}(t) = 2(G_H(t) - G_H(0)) + 2 &\int_0^t \big(Q_H(s) + \varepsilon_p^2 T_{p,H}(s) \big) \, \mathrm{d}s \\ &+ \frac{E_0}{2} \big(\|D_{-y} E_{u_1,H}(0)\|_{y,+}^2 + \|D_{-x} E_{u_2,H}(0)\|_{x,+}^2 \big) + E_0 (D_{c,x} E_{u_1,H}(0), D_{c,y} E_{u_2,H}(0))_H \end{aligned}$$

and

$$C_1 = \max \left\{ \varepsilon_Q^2, C\varepsilon_p^2 + \frac{2(1 + C_{qu})}{\varepsilon_p^2} \right\}.$$

We now estimate the terms $\tilde{S} = -E_0 (D_{c,x} E_{u_1,H}(t), D_{c,y} E_{u_2,H}(t))_H$ and $S_{u,H}(t)$.

- Estimate for $\tilde{S}$:

  Combining the Cauchy-Schwarz and Proposition 5, we have

  $$|\tilde{S}| \leq \frac{E_0}{2} \big(\|D_{-x} E_{u_1,H}(t)\|_{x,+}^2 + \|D_{-y} E_{u_2,H}(t)\|_{y,+}^2 \big).$$

- Estimate for $S_{u,H}(t)$:

  We start by observing that following the construction of the estimate for $Q_H(t)$ in Proposition 7, it can be shown that there exists a positive constant C_2, H and t independent, such that, for all $\varepsilon_G \neq 0$ and $t \geq 0$,

  $$\begin{aligned} G_H(t) \leq C_2 &\sum_{\Delta \in \mathcal{T}_H} \operatorname{diam}^4(\Delta) \Big(\|\mathbf{u}''(t)\|^2_{[H^2(\Delta)]^2} + \|\mathbf{u}(t)\|^2_{[H^3(\Delta)]^2} + \|p(t)\|^2_{H^3(\Delta)} \Big) \\ &+ \varepsilon_G^2 \|\nabla_H E_{\mathbf{u},H}(t)\|_+^2. \end{aligned} \tag{44}$$

  Taking into account the estimate from inequality (44) and the estimates obtained before for $Q_H(t)$ and $T_{p,H}(t)$, (38) and (36), respectively, for $S_{u,H}(t)$ we deduce that there exists a positive

constant C_3, H and t independent, such that

$$
\begin{aligned}
|S_{u,H}(t)| \leq C_3 \sum_{\Delta\in\mathcal{T}_H} \operatorname{diam}^4(\Delta) \Big[&\|\mathbf{u}''(t)\|^2_{[H^2(\Delta)]^2} + \|\mathbf{u}(t)\|^2_{[H^3(\Delta)]^2} + \|p(t)\|^2_{H^3(\Delta)} \\
&+ \int_0^t \|\mathbf{u}'''(s)\|^2_{[H^2(\Delta)]^2} + \|\mathbf{u}'(s)\|^2_{[H^3(\Delta)]^2} + \|p'(s)\|^2_{H^3(\Delta)} + \|p(s)\|^2_{H^3(\Delta)} \,\mathrm{d}s \\
&+ \int_0^t \|q(p(s))\|^2_{H^2(\Delta)} \,\mathrm{d}s \Big] \\
&+ C_3 \sum_{\Delta\in\mathcal{T}_H} \operatorname{diam}^4(\Delta) \Big(\|\mathbf{u}''(0)\|^2_{[H^2(\Delta)]^2} + \|\mathbf{u}(0)\|^2_{[H^3(\Delta)]^2} + \|p(0)\|^2_{H^3(\Delta)} \Big) \\
&+ \left(\frac{E_0}{2} + \varepsilon_G^2 \right) \|\nabla_H E_{\mathbf{u},H}(0)\|^2_+ + C_3 \varepsilon_G^2 \|\nabla_H E_{\mathbf{u},H}(t)\|^2_+ .
\end{aligned}
$$

Combining the last estimate with inequality (43) we get

$$
\|E'_{\mathbf{u},H}(t)\|^2_H + \left(\frac{E_0}{2} - C_3\varepsilon_G^2 \right) \|\nabla_H E_{\mathbf{u},H}(t)\|^2_+ \leq A_{u,0}(t) + 2C_1 \int_0^t \left(\|\nabla_H E_{\mathbf{u},H}(s)\|^2_+ + \|E'_{\mathbf{u},H}(s)\|^2_H \right) \mathrm{d}s,
$$

where

$$
\begin{aligned}
A_{u,0}(t) = \|E'_{\mathbf{u},H}(0)\|^2_H &+ \left(\frac{E_0}{2} + \varepsilon_G^2 \right) \|\nabla_H E_{\mathbf{u},H}(0)\|^2_+ \\
&+ C_3 \sum_{\Delta\in\mathcal{T}_H} \operatorname{diam}^4(\Delta) \Big[\|\mathbf{u}''(t)\|^2_{[H^2(\Delta)]^2} + \|\mathbf{u}(t)\|^2_{[H^3(\Delta)]^2} + \|p(t)\|^2_{H^3(\Delta)} + \\
&+ \int_0^t \|\mathbf{u}'''(s)\|^2_{[H^2(\Delta)]^2} + \|\mathbf{u}'(s)\|^2_{[H^3(\Delta)]^2} + \|p'(s)\|^2_{H^3(\Delta)} + \|p(s)\|^2_{H^3(\Delta)} + \|q(p(s))\|^2_{H^2(\Delta)} \,\mathrm{d}s \\
&+ \|\mathbf{u}''(0)\|^2_{[H^2(\Delta)]^2} + \|\mathbf{u}(0)\|^2_{[H^3(\Delta)]^2} + \|p(0)\|^2_{H^3(\Delta)} \Big] .
\end{aligned}
$$

Choosing ε_G such that $\frac{E_0}{2} - C_3\varepsilon_G^2 > 0$ and applying Gronwall's lemma, we conclude that

$$
\|E'_{\mathbf{u},H}(t)\|^2_H + \|\nabla_H E_{\mathbf{u},H}(t)\|^2_+ \lesssim \|E'_{\mathbf{u},H}(0)\|^2_H + \|\nabla_H E_{\mathbf{u},H}(0)\|^2_+ + T_{\mathbf{u}}(t),
$$

for $t \in [0,T]$, where

$$
\begin{aligned}
|T_{\mathbf{u}}(t)| \lesssim \sum_{\Delta\in\mathcal{T}_H} \operatorname{diam}^4(\Delta) \Big[&\|\mathbf{u}\|^2_{H^3(0,T;[H^2(\Delta)]^2)} + \|\mathbf{u}\|^2_{H^1(0,T;[H^3(\Delta)]^2))} + \|p\|^2_{H^1(0,T;H^3(\Delta))} + \\
&+ \|q(p)\|^2_{H^1(0,T;H^2(\Delta))} + \|\mathbf{u}''(0)\|^2_{[H^2(\Delta)]^2} + \|\mathbf{u}(0)\|^2_{[H^3(\Delta)]^2} + \|p(0)\|^2_{H^3(\Delta)} \Big] .
\end{aligned}
$$

Combining the previous estimate with the estimate for $\|\nabla_H E_{p,H}(t)\|^2_+$ from Proposition 6 concludes the proof. □

An immediate consequence of Theorem 1 is the order of convergence for the semidiscrete displacement and pressure approximations.

Corollary 1 (Quadratic convergence for displacement and pressure)**.** *Given the conditions in Theorem 1, if* $\|E'_{\mathbf{u},H}(0)\|_H \lesssim H^2_{\max}$ *and* $\|\nabla_H E'_{\mathbf{u},H}(0)\|_+ \lesssim H^2_{\max}$*, then*

$$
\|E'_{\mathbf{u},H}(t)\|_H + \|\nabla_H E_{\mathbf{u},H}(t)\|_+ + \|\nabla_H E_{p,H}(t)\|_+ \lesssim H^2_{\max}
$$

and

$$
\|E_{\mathbf{u},H}(t)\|_H \lesssim H^2_{\max}.
$$

We can also obtain an uniform bound for the semidiscrete displacement's velocity approximation as a consequence of Theorem 1.

Corollary 2 (Uniform bound for $\|\mathbf{u}'_H(t)\|_{H,\infty}$)**.** *Let u_H denote the semidiscrete approximation of the displacement defined by (23), (24) and (28). Under the assumptions of Theorem 1,*

$$\|\mathbf{u}'_H(t)\|_{H,\infty} \lesssim 1,$$

for all $t \in [0,T]$.

After establishing the convergence for the displacement and pressure approximations, we now present error estimates for the concentration approximations. Let $E_{b,H}(t)$ and $E_{c,H}(t)$ denote the spatial discretization errors for the semidiscrete approximations $b_H(t)$ and $c_H(t)$, respectively, defined by (25)-(27) and

$$\mathbb{E}_w(t) = \|E_{w,H}(t)\|_H^2 + \int_0^t \|\nabla_H E_{w,H}(s)\|_+^2 \,\mathrm{d}s,$$

for $w = b, c$ and $t \in [0,T]$.

Theorem 2 (Estimate for the cell densities error)**.** *If the conditions of Theorem 1 hold,*

$$\frac{15}{2} L_\phi^2 (2C_{qu}+1)^2 \|b\|^2_{C^1([0,T];C(\overline{\Omega}))} < D_{c,0} D_{b,0}$$

and the solution of system of equations (1) to (4) satisfies $b, c \in C^1([0,T]; C(\overline{\Omega})) \cap L^2(0,T; H^3(\Omega) \cap H_0^1(\Omega)) \cap H^1(0,T; H^2(\Omega))$, $\mathbf{u}'b, \mathbf{u}'c \in [L^2(0,T; H^2(\Omega))]^2$, $\phi(\nabla c, c, \nabla p)b, \psi(\nabla p)c \in [L^2(0,T; H^2(\Omega))]^2$, then

$$\mathbb{E}_b(t) + \mathbb{E}_c(t) \lesssim \|E_{b,H}(0)\|_H^2 + \|E_{c,H}(0)\|_H^2 + \int_0^t T_H(s)\,\mathrm{d}s, \tag{45}$$

for $t \in [0,T]$, where $T_H(s)$ satisfies

$$\begin{aligned} |T_H(t)| \lesssim\ & T_{b,c}(t) + \gamma_{b,c}(t)\big(\|E'_{\mathbf{u},H}(0)\|_H^2 + \|\nabla_H E_{\mathbf{u},H}(0)\|_+^2\big) \\ & + \sum_{\Delta \in \mathcal{T}_H} \operatorname{diam}^4(\Delta) \Big(\|\mathbf{u}\|^2_{[H^3(0,T;H^2(\Delta))]^2} + \|\mathbf{u}\|^2_{[H^1(0,T;H^3(\Delta))]^2} + \|p\|^2_{H^1(0,T;H^3(\Delta))} \\ & + \|q(p)\|^2_{L^2(0,T;H^2(\Delta))} + \|\mathbf{u}''(0)\|^2_{[H^2(\Delta)]^2} + \|\mathbf{u}(0)\|^2_{[H^3(\Delta)]^2} + \|p(0)\|^2_{H^3(\Delta)} \Big). \end{aligned} \tag{46}$$

with

$$\gamma_{b,c}(t) = \frac{(2C_{qu}+1)^2}{2} \left(\frac{3L_\phi^2}{\epsilon_b^2} \|b(t)\|^2_{H^2(\Omega)} + \frac{L_\psi^2}{\epsilon_c^2} \|c(t)\|^2_{H^2(\Omega)} \right) + \frac{1}{\epsilon_b^2} \|b(t)\|^2_{H^2(\Omega)}$$

and

$$\begin{aligned} T_{b,c}(t) = & \sum_{\Delta \in \mathcal{T}_H} \operatorname{diam}^4(\Delta) \left(\sum_{r=b',c',f,g} \|r(t)\|^2_{H^2(\Delta)} + \sum_{r=b,c} \Big(\|r(t)\|^2_{H^3(\Delta)} + \|\mathbf{u}'(t) r(t)\|^2_{[H^2(\Delta)]^2} \Big) \right. \\ & + \sum_{r=b,c} \|r(t)\|^2_{W^{1,\infty}(\Delta)} \left(\sum_{r=b,c} \|r(t)\|^2_{H^2(\Delta)} + \|p(t)\|^2_{H^3(\Delta)} \right) + \|b(t)c(t)\|^2_{H^3(\Delta)} \\ & \left. + \|\phi(\nabla c(t), c(t), \nabla p(t)) b(t)\|^2_{[H^2(\Delta)]^2} + \|\psi(\nabla p(t)) c(t)\|^2_{[H^2(\Delta)]^2} + \sum_{r=b,c} \|r(t) p(t)\|^2_{H^3(\Delta)} \right). \end{aligned}$$

Proof. With the regularity conditions from Section 2.7 and following [11], it can be shown that, for all $\epsilon_b \neq 0$,

$$\begin{aligned}
&\frac{1}{2}\frac{\mathrm{d}}{\mathrm{d}t}\|E_{b,H}(t)\|_H^2 + \left(D_{b,0} - \frac{5}{2}\epsilon_b^2\right)\|\nabla_H E_{b,H}(t)\|_+^2 \\
&\qquad \leq \frac{3L_\phi^2}{2\epsilon_b^2}\|b(t)\|_{H^2(\Omega)}^2(2C_{qu}+1)^2\big(\|E_{c,H}(t)\|_{1,H}^2 + \|\nabla_H E_{p,H}(t)\|_+^2\big) \\
&\qquad\quad + \frac{1}{\epsilon_b^2}\left(C_\phi^2 + \frac{1}{2}\|\mathbf{u}_H'(t)\|_{H,\infty}^2\right)\|E_{b,H}(t)\|_H^2 + \frac{1}{2\epsilon_b^2}\|b(t)\|_{H^2(\Omega)}^2\|E_{\mathbf{u},H}'(t)\|_H^2 \\
&\qquad\quad + \frac{2L_{D_b}^2}{\epsilon_b^2}\|b(t)\|_{H^2(\Omega)}^2\big(\|E_{b,H}(t)\|_H^2 + \|E_{c,H}(t)\|_H^2\big) \\
&\qquad\quad + L_f(\|E_{b,H}(t)\|_H + \|E_{c,H}(t)\|_H)\|E_{b,H}(t)\|_H + T_{b,H}(t),
\end{aligned} \tag{47}$$

with

$$\begin{aligned}
T_{b,H}(t) = C_1 \sum_{\Delta\in\mathcal{T}_H} \mathrm{diam}^4(\Delta)\Bigg(&\sum_{r=f,b'}\|r(t)\|_{H^2(\Delta)}^2 + \|b(t)\|_{H^3(\Delta)}^2 + \|\mathbf{u}'(t)b(t)\|_{[H^2(\Delta)]^2}^2 \\
&+ \|b(t)\|_{W^{1,\infty}(\Delta)}^2\Big(\|b(t)\|_{H^2(\Delta)}^2 + \|c(t)\|_{H^2(\Delta)}^2\Big) \\
&+ \|\phi(\nabla c(t), c(t), \nabla p(t))b(t)\|_{[H^2(\Delta)]^2}^2 \\
&+ \sum_{r=c,p}\|b(t)\|_{W^{1,\infty}(\Delta)}^2\|r(t)\|_{H^3(\Delta)}^2 + \|r(t)b(t)\|_{H^3(\Delta)}^2\Bigg),
\end{aligned} \tag{48}$$

for some positive constant C_1, H and t independent. Since a similar estimate is obtained for $E_{c,H}(t)$, we can conclude that

$$\begin{aligned}
&\frac{\mathrm{d}}{\mathrm{d}t}\big(\|E_{b,H}(t)\|_H^2 + \|E_{c,H}(t)\|_H^2\big) + 2\left(D_{b,0} - \frac{5\epsilon_b^2}{2}\right)\|\nabla_H E_{b,H}(t)\|_+^2 \\
&\qquad\qquad + 2\left(D_{c,0} - \frac{3}{2\epsilon_c^2} - \frac{3L_\phi^2}{2\epsilon_b^2}\|b(t)\|_{C(\overline{\Omega})}^2(2C_{qu}+1)^2\right)\|\nabla_H E_{c,H}(t)\|_+^2 \\
&\qquad\qquad \leq \theta_{b,c}(t)\big(\|E_{b,H}(t)\|_H^2 + \|E_{c,H}(t)\|_H^2\big) + T_H(t),
\end{aligned} \tag{49}$$

where

$$\begin{aligned}
\theta_{b,c}(t) &= 4\Big(L_{D_b}\|b(t)\|_{C(\overline{\Omega})}^2 + L_{D_c}\|c(t)\|_{C(\overline{\Omega})}^2 + \max\{L_f, L_g\}\Big) \\
&\quad + \max\left\{\frac{2}{\epsilon_b^2}\left(C_\psi^2 + \frac{1}{2}\|\mathbf{u}_H'(t)\|_{H,\infty}^2\right), \frac{2}{\epsilon_c^2}\left(C_\phi^2 + \frac{1}{2}\|\mathbf{u}_H'(t)\|_{H,\infty}^2\right) + \frac{3L_\phi^2}{\epsilon_b^2}\|b(t)\|_{C(\overline{\Omega})}^2(2C_{qu}+1)^2\right\}, \\
T_H(t) &= T_{b,c}(t) + \gamma_{b,c}(t)\big(\|\nabla_H E_{p,H}(t)\|_+^2 + \|E_{\mathbf{u},H}'(t)\|_H^2\big).
\end{aligned}$$

Using Theorem 1, there exists a positive constant C_3, H and t independent, such that

$$\begin{aligned}
|T_H(t)| \leq T_{b,c}(t) + C_3\gamma_{b,c}(t)\Big(&\|E_{\mathbf{u},H}'(0)\|_H^2 + \|\nabla_H E_{\mathbf{u},H}(0)\|_+^2 \\
&+ \sum_{\Delta\in\mathcal{T}_H}\mathrm{diam}^4(\Delta)\Big(\|\mathbf{u}\|_{[H^3(0,T;H^2(\Delta))]^2}^2 + \|\mathbf{u}\|_{[H^1(0,T;H^3(\Delta))]^2}^2 + \|p\|_{H^1(0,T;H^3(\Delta))}^2 \\
&+\|q(p)\|_{L^2(0,T;H^2(\Delta))}^2 + \|\mathbf{u}''(0)\|_{[H^2(\Delta)]^2}^2 + \|\mathbf{u}(0)\|_{[H^3(\Delta)]^2}^2 + \|p(0)\|_{H^3(\Delta)}^2\Big)\Big).
\end{aligned}$$

The proof is concluded observing that inequality (49) leads to

$$\|E_{b,H}(t)\|_H^2 + \|E_{c,H}(t)\|_H^2 + \int_0^t e^{\int_0^s \theta_{b,c}(\tau)\,\mathrm{d}\tau}\big((2D_{b,0} - 5\epsilon_b^2)\|\nabla_H E_{b,H}(s)\|_+^2 + (2D_{c,0} - \theta(s))\|\nabla_H E_{c,H}(s)\|_+^2\big)\,\mathrm{d}s \leq e^{\int_0^t \theta_{b,c}(\tau)\,\mathrm{d}\tau}\big(\|E_{b,H}(0)\|_H^2 + \|E_{c,H}(0)\|_H^2\big) + \int_0^t e^{\int_0^s \theta_{b,c}(\tau)\,\mathrm{d}\tau} T_H(s)\,\mathrm{d}s,$$

for $t \in [0,T]$, with $\theta(t) = \frac{3}{\epsilon_c^2} + \frac{3}{\epsilon_b^2}L_\phi^2\|b(t)\|_{C(\overline{\Omega})}^2(2C_{qu}+1)^2$ and choosing ϵ_b and ϵ_b such that $D_{c,0} - \frac{3}{2\epsilon_c^2} - \frac{3L_\phi^2}{2\epsilon_b^2}(2C_{qu}+1)^2\|b\|_{C^1([0,T];C(\overline{\Omega}))}^2 > 0$ and $2D_{b,0} - 5\epsilon_b^2 > 0$. □

Corollary 3 (Quadratic convergence of scheme)**.** *Under the assumptions of Corollary 1 and Theorem 2, if the initial data b_0 and c_0 is approximated with an error of order $H_{\max}^2$, then*

$$\|E_{b,H}(t)\|_H^2 + \|E_{c,H}(t)\|_H^2 + \int_0^t \big(\|\nabla_H E_{b,H}(s)\|_+^2 + \|\nabla_H E_{c,H}(s)\|_+^2\big)\,\mathrm{d}s \lesssim H_{\max}^4,$$

for $t \in [0,T]$.

Remark 4. Corollaries 1 and 3 show that the proposed finite difference method for the displacement-pressure and concentration problems have second-order convergence in space, provided that the solution of the continuous problem is smooth enough and the discrete initial data is of second-order. Our technique requires a uniform bound assumption for the discrete displacement velocity $\mathbf{u}_H'(t)$, which is ensured by Corollary 2 as a consequence of Theorem 1 and suitable approximations for the initial data. This boundedness assumption is crucial to handle the nonlinear convection terms in the equations for b and c.

4 Numerical Simulations

We have two objectives in this section: (i) to numerically illustrate the results obtained in this previous section and (ii) to numerically simulate an academic example for tumor cell migration. We start by presenting an example which will allow us to analyze the convergence rates, with respect to space, given by Corollaries 1 and 3.

4.1 Convergence rate in space and time

We introduce now the necessary notations to present a fully discrete implicit-explicit (IMEX) scheme for the displacement-pressure and concentration problems. In $[0,T]$, we introduce the uniform time grid $\{t_n,\, n = 0,\ldots,\mathcal{N}\}$, where $t_0 = 0$, $T_{\mathcal{N}} = T$ and $t_n = t_{n-1} + \Delta t, n = 1,\ldots,\mathcal{N}$. We denote by $\mathbf{u}_H^n = (u_{H,1}^n, u_{H,2}^n)$, p_H^n, b_H^n and c_H^n the numerical approximations for $\mathbf{u}_H(t_n) = (u_{H,1}(t_n), u_{H,2}(t_n))$, $p_H(t_n)$, $b_H(t_n)$ and $c_H(t_n)$, respectively.

The diffusion tensors at time t_n are approximated by

$$D_{p,H}^n = D_p(p_H^n), \quad D_{b,H}^{n,n+1} = D_b(b_H^n, c_H^{n+1}), \quad D_{c,H}^n = D_c(b_H^n, c_H^n),$$

the convection terms are approximated by

$$\phi_H^n = \phi(\nabla_H c_H^n, c_H^n, \nabla_H p_H^n), \quad \psi_H^n = \psi(\nabla_H p_H^n)$$

and the source terms are approximated by

$$f_H^{n,n+1} = f(b_H^n, c_H^{n+1}), \quad g_H^n = g(b_H^n, c_H^n).$$

We consider the following IMEX finite difference problem: for $n = 1, \ldots, \mathcal{N}-1$, find $\mathbf{u}_H^n \in [V_{H,0}]^2$, b_H^n, $c_H^n \in V_{H,0}$, $p_H^n \in V_H$ such that $p_H^n = R_H p_1(t_n)$ on $\Gamma_{1,H}$, $p_H^n = R_H p_2(t_n)$ on $\Gamma_{2,H}$,

$$\begin{cases} q_H^{n+1} = -\nabla_H^* \cdot \big(D_{p,H}^n \nabla_H p_H^{n+1}\big) + \nabla_{c,H} \cdot (D_{-t}\mathbf{u}_H^n), & (50) \\ \dfrac{u_{H,1}^{n+1} - 2u_{H,1}^n + u_{H,1}^{n-1}}{\Delta t^2} = \nabla_H^* \cdot \Big(E_0 \nabla_H u_{H,1}^{n+1}\Big) + \dfrac{E_0}{2} D_{c,x} D_{c,y} u_{H,2}^n - D_h p_H^{n+1}, & (51) \\ \dfrac{u_{H,2}^{n+1} - 2u_{H,2}^n + u_{H,2}^{n-1}}{\Delta t^2} = \nabla_H^* \cdot \Big(E_0 \nabla_H u_{H,2}^{n+1}\Big) + \dfrac{E_0}{2} D_{c,y} D_{c,x} u_{H,1}^n - D_k p_H^{n+1}, & (52) \\ D_{-t} c_H^{n+1} + \nabla_{c,H} \cdot \big(\big(\psi_H^{n+1} + D_{-t}\mathbf{u}_H^n\big) c_H^{n+1}\big) = \nabla_H^* \cdot \big(D_{c,H}^n \nabla_H c_H^{n+1}\big) + g_H^n, & (53) \\ D_{-t} b_H^{n+1} + \nabla_{c,H} \cdot \big(\big(\phi_H^{n+1} + D_{-t}\mathbf{u}_H^n\big) b_H^{n+1}\big) = \nabla_H^* \cdot \Big(D_{b,H}^{n,n+1} \nabla_H b_H^{n+1}\Big) + f_H^{n,n+1}, & (54) \end{cases}$$

in $\overline{\Omega}_H$, with homogeneous Dirichlet boundary conditions and initial conditions

$$\mathbf{u}_H^1 = R_H(\mathbf{h}_2 + \Delta t\, \mathbf{h}_1), \quad \mathbf{u}_H^0 = R_H \mathbf{h}_2, \quad b_H^0 = R_H b_0 \quad \text{and} \quad c_H^0 = R_H c_0.$$

4.2 Accuracy of numerical solutions

In what follows we compute the fully discrete in time and space errors. Taking $E_{\mathbf{u},H}^n = R_H \mathbf{u}(t_n) - \mathbf{u}_H^n$, $E_{b,H}^n = R_H b(t_n) - b_H^n$, $E_{c,H}^n = R_H c(t_n) - c_H^n$, $E_{p,H}^n = R_H p(t_n) - p_H^n$, $n = 0, \ldots, \mathcal{N}$, we define

$$Error_{b,c,H} = \max_{n=0,\ldots,\mathcal{N}-1} \Big\{ \|E_{b,H}^{n+1}\|_{1,H}^2 + \|E_{c,H}^{n+1}\|_{1,H}^2 \Big\},$$

as the error associated with the discretization of the density of cells and the concentration of chemical signal and

$$Error_{p,\mathbf{u},H} = \max_{n=0,\ldots,\mathcal{N}-1} \Big\{ \|E_{\mathbf{u},H}^{n+1}\|_{1,H}^2 + \|\nabla_H E_{p,H}^{n+1}\|_+^2 \Big\},$$

as the error associated with the discretization of the pressure equation and the displacement. For the numerical simulation we set $\Omega = [0,1]^2$ and $T = 1$. We consider the timestep of order $H_{\min}^2$ which allow us to neglect the discretization error in time. For the coefficient functions we consider

$$D_b = \begin{bmatrix} 2 + cb & 0 \\ 0 & 2 + b^2 \end{bmatrix}, \quad D_c = \begin{bmatrix} 2 + c + b & 0 \\ 0 & 2 + c^2 \end{bmatrix}, \quad D_p = \begin{bmatrix} 1 + p^2 & 0 \\ 0 & 1 + 2p^2 \end{bmatrix},$$

and

$$\phi = (\nabla(p + c) + c), \quad \psi = (\nabla p).$$

The initial conditions and the source functions are such that the exact solution of equations (1) to (8), is given by

$$\begin{aligned} b(x,y,t) &= e^{5t} xy(x-1)(y-1)|y-0.5|^\alpha, & c(x,y,t) &= e^{5t} xy(x-1)(y-1)|y-0.3|^\alpha, \\ p(x,y,t) &= 50xy(x-1)(y-1)|y-0.7|^\alpha, & u_i(x,y,t) &= e^t xy \sin(\pi x)\sin(\pi y)|y-0.5|^\alpha, \end{aligned}$$

for $i = 1, 2$ and $\alpha \in \mathbb{R}$. We highlight that the solution $(b, c, p, \mathbf{u})$ satisfies the regularity assumptions of Theorems 1 and 2 with $\alpha = 3.1$.

In order to illustrate the convergence rates we repeatedly consider nonuniform grids which are randomly generated with $H_{\max}$ between 0.020 and 0.0795. For each grid we plot the logarithm of errors $Error_{b,c,H}$ and $Error_{p,\mathbf{u},H}$ *versus* the logarithm of $H_{\max}$. Additionally, we also plot the fitting least square fitting line and indicate its slope. As shown in Figure 1, the slope is close to two in both

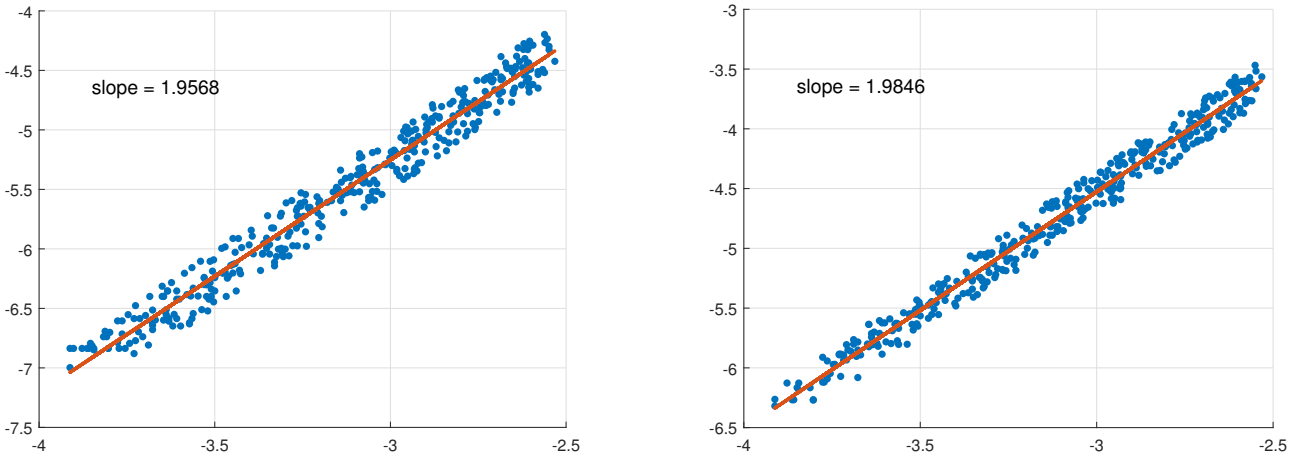

Figure 1: Log-log plots of $Error_{b,c,H}$ (on the left) and $Error_{p,\mathbf{u},H}$ (on the right) versus $H_{\max}$. The best fitting least square line is plotted in orange.

cases, which illustrates our theoretical results.

4.3 Cancer cell migration: modeling and simulation

4.4 *Introduction* effect

It is well accepted the importance of the lymphatic system in cancer cell migration. Cell migration towards the lymphatic capillaries depends on several factors, as for instance, the chemokines gradient, the characteristics of the extracellular matrix, lymphatic endothelial cells and fluid flow. In [29] an in vitro experiment is reported to illustrate the role of interstitial fluid flow from blood to lymphatic capillaries in cancer cell migration. The authors considered CCL21 (CC Chemokine Ligand 21) as chemoattractant and MDA-MB-435S tumor cells. The cells were distributed into Matrigel® used to simulate the extracellular matrix and a water flow was considered to simulate the interstitial fluid flow.

To describe cell migration in a human tissue $\Omega = (0,1)^2$ enhanced by a chemoattractant gradient, interstitial fluid flow whose fluid pressure induces a displacement, we consider the following simplified version of the differential system (1)-(4)

$$\begin{cases} \dfrac{\partial b}{\partial t} + \nabla\cdot\left(\phi b\nabla c - Kb\nabla p + \dfrac{\partial \mathbf{u}}{\partial t}b\right) = D_b\Delta b, & (55)\\ \dfrac{\partial c}{\partial t} + \nabla\cdot\left(-Kc\nabla p + \dfrac{\partial \mathbf{u}}{\partial t}c\right) = D_c\Delta c, & (56)\\ -\nabla\cdot\left(K\nabla p + \dfrac{\partial \mathbf{u}}{\partial t}\right) = q, & (57)\\ \dfrac{\partial^2 \mathbf{u}}{\partial t^2} = \boldsymbol{\nabla}\cdot(E_0\boldsymbol{\varepsilon}(\mathbf{u})) - \nabla p & (58) \end{cases}$$

defined in $\Omega\times(0,T]$. In (55)-(58), b denotes the cell density, c the chemoattractant concentration, p the fluid pressure and $\mathbf{u} = (u_1, u_2)$ the displacement field of the medium. We recall that, in the

pressure equation, q represents a source term and K is the hydraulic conductivity. The flow conditions are modeled by the following localized source term

$$q = \begin{cases} q_0, \text{ if } (x-0.5)^2 + (y-0.3)^2 < 0.01^2, \\ 0, \text{ otherwise,} \end{cases} \tag{59}$$

where q_0 is a constant source parameter.

In (55), D_b is the cell diffusivity and ϕb represents chemotactic sensitivity to the chemoattractant, while, in (56), D_c, denotes the diffusion coefficient of the chemoattractant. The term $\nabla\cdot(-Kc\nabla p)$ describes the chemoattractant transport under flow conditions. The velocity of cells and chemical signal induced by the displacement are described by the convection terms $\nabla\cdot\left(\frac{\partial \mathbf{u}}{\partial t}b\right)$ and $\nabla\cdot\left(\frac{\partial \mathbf{u}}{\partial t}c\right)$, respectively. The Young modulus E_0 in (58) quantifies the stiffness of the material.

The parameters, units, description, reference values and chosen simulation values are summarized in Table 1, where the simulation values are taken as typical reference values from the literature. We assume, without loss of generality, that $K = 1$ and we also set $q_0 = 22\,\mathrm{h}^{-1}$, which yields typical values for the interstitial velocity in the range of $0.36\,\mathrm{mm\,h}^{-1}$ to $7.2\,\mathrm{mm\,h}^{-1}$. No fixed value is presented for the Young's modulus, as we intend to analyze the effects of varying tissue stiffness.

Remark 5 (Young modulus of human tissue). The Young's modulus of human tissue varies widely. Soft tissues like lung, breast and brain typically have stiffness values in the ranges of 25 kPa to 35 kPa, 4 kPa to 12 kPa and 7 kPa to 26 kPa, respectively. In contrast, bone tissue and skin tissue affected by tumours are significantly stiffer, with a Young's modulus that can exceed 689 MPa and be around 400 kPa, respectively. For a comprehensive list of values for normal and cancerous tissues, we refer to [37, Table 6.1]. In this work, we focus on softer tissues and adopt a Young's modulus in the range of 1.6 kPa to 30 kPa.

Parameter	Description	Unit	Reference values	Value
D_b	Cell diffusion coefficient	$\mathrm{mm^2\,h^{-1}}$	$[3.6\times10^{-6}, 3.6\times10^{-4}]$	5.3×10^{-4}
D_c	Chemoattractant diffusion coefficient	$\mathrm{mm^2\,h^{-1}}$	$[3.6\times10^{-4}, 3.6\times10^{-1}]$	2.6×10^{-3}
ϕ	*Chemotaxis* coefficient	$\mathrm{mm^2\,h^{-1}}$	[0.001, 1]	0.07
K	Hydraulic conductivity	$\mathrm{mm^2\,Pa^{-1}\,h^{-1}}$	-	1
q_0	Flow source term	$\mathrm{h^{-1}}$	-	22
E_0	Young's modulus	MPa	[0.0016, 0.03]	-

Table 1: Parameters for the system of (55)-(58).

Initially, we set cancer cells concentrated in a region of higher density compared to the chemoattractant:

$$b(x,y,0) = 0.8\,e^{-\frac{(x-0.4)^2+(y-0.7)^2}{0.01}} \quad \text{and} \quad c(x,y,0) = 0.5\,e^{-\frac{(x-0.6)^2+(y-0.6)^2}{0.04^2}},$$

for $(x,y) \in \overline{\Omega}$.

In the numerical simulations, we use the fully discrete scheme defined by (50)-(54) using a uniform mesh with $H_{\max} = H_{\min} = 1.25\times10^{-2}$ and time step $\Delta t = 2\times10^{-2}$. Figure 2 illustrates the computational domain and initial density of cells and concentration of chemical signal.

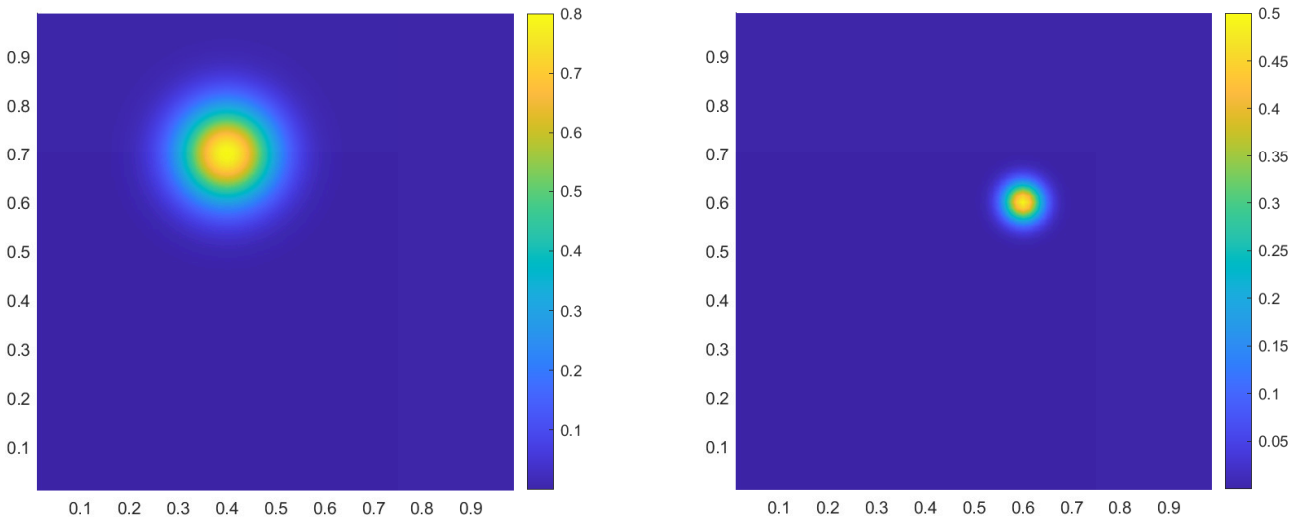

(a) Initial cell density, b.

(b) Initial chemical signal concentration, c.

Figure 2: Representation of the computational domain and initial conditions for the cell density and chemical signal concentration.

We now explore several simulation scenarios. Initially, in Section 4.5, we consider a simplified case where diffusion occurs and without fluid pressure or tissue displacement, focusing solely on *chemotaxis*. Next, in Section 4.6, we incorporate fluid pressure to evaluate its influence. After that, we combine all mechanisms in Section 4.7, *chemotaxis*, fluid pressure and displacement, in order to study their combined impact on cell movement. We also consider in Section 4.8 an additional scenario in which the displacement field is generated by a source term that continuously emits mechanical waves. This setup is intended to mimic the effect of ultrasound waves propagated through the tissue, commonly used in therapeutic contexts such as targeted drug delivery. Our goal is to investigate how this persistent mechanical stimulation influences the migration of cancer cells. For these cases, all parameters will be given by the values in Table 1. However, in same cases, we intend to analyze some variations of the parameters of the model. All simulations were run for 15 h.

As a final note before presenting the simulations, we aim to quantify the percentage of migrated cells under the influence of each component individually. Specifically, we evaluate the migration resulting from *chemotaxis* alone, *chemotaxis* coupled with fluid flow and the combination of all three mechanisms. In these measurements, we isolate the effects of each mechanism by excluding the contribution of diffusion to cell movement. To achieve this, we adopt a domain partition where we define a chamber region and measure the percentage of cells that migrate into this area.

4.5 *Chemotaxis* effect

When considering only the effect of *chemotaxis* on cell movement, we expect cells to move towards the higher chemical concentration and anticipate a gradual migration towards southeast. This behavior is illustrated in Figure 3, which plots the cell density, b, at different time levels, overlaid with contour lines representing the initial distribution for reference. Figure 3 also shows a small accumulation of cells near the region of high chemical concentration at early times. As time progresses, the cell density at the original location decreases, while cells continue to migrate southeast. At later time instances, the

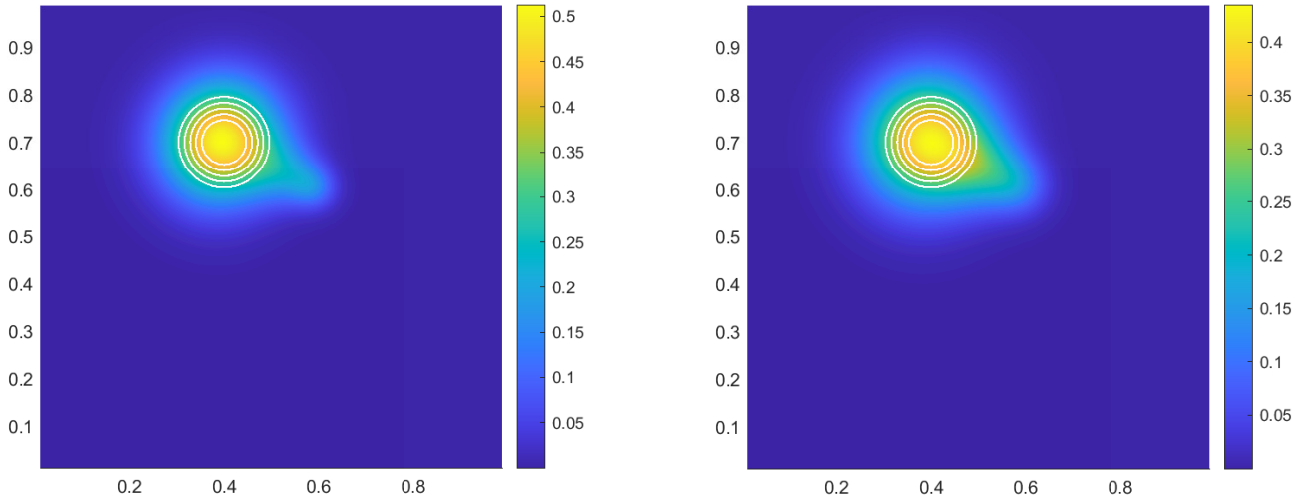

(a) $t = 2\,\mathrm{h}$

(b) $t = 3\,\mathrm{h}$

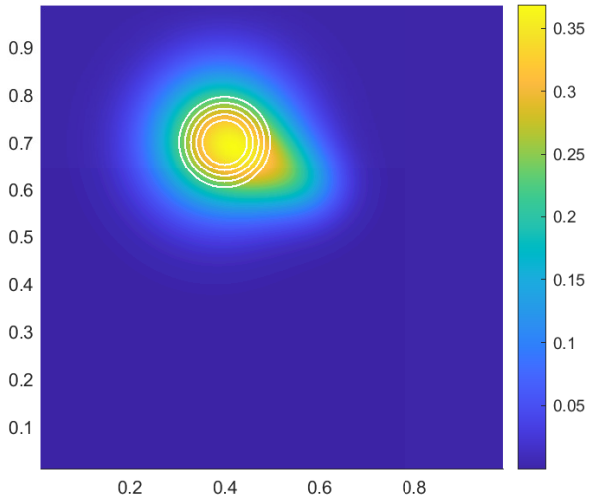

(c) $t = 5\,\mathrm{h}$

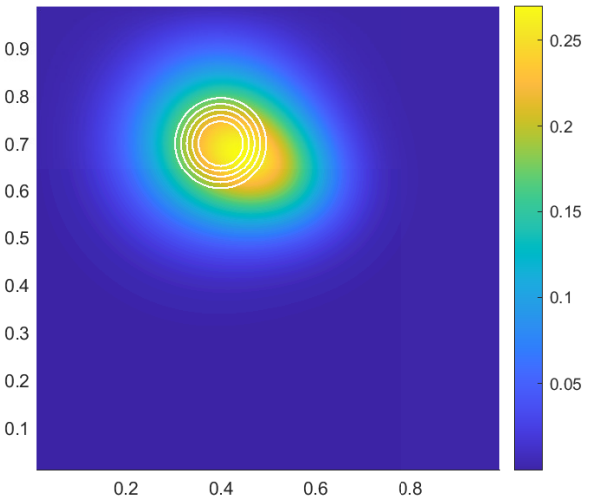

(d) $t = 9\,\mathrm{h}$

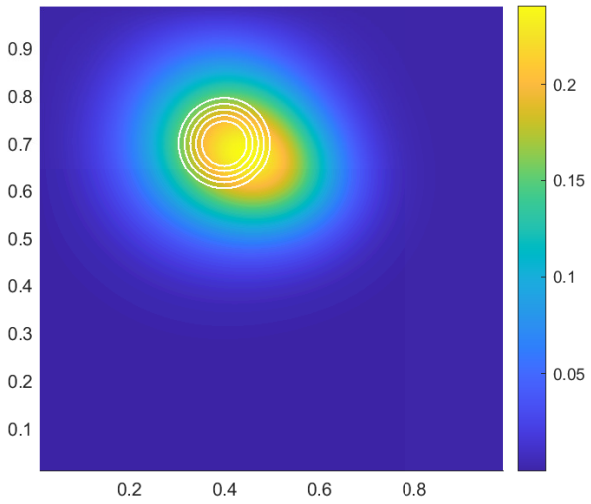

(e) $t = 11\,\mathrm{h}$

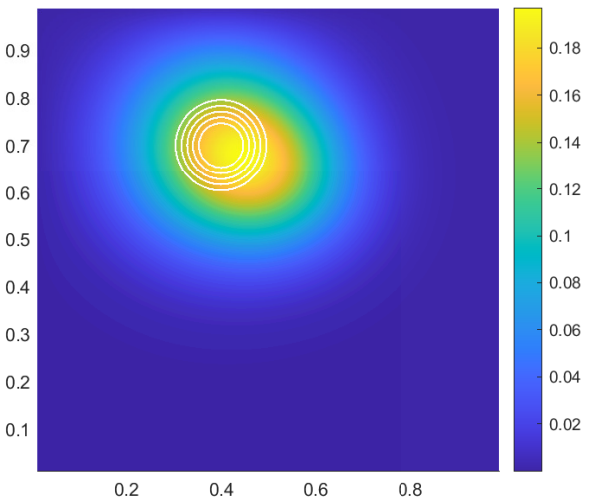

(f) $t = 15\,\mathrm{h}$

Figure 3: Cancer cell distribution under *chemotaxis* at different time levels.

movement becomes less pronounced and diffusion begins to dominate the overall dynamics. Regarding the concentration of the chemical signal, c, we expect diffusion to be the only dynamic process, since

in this case the governing equation is a pure diffusion equation without any source terms. Figure 4

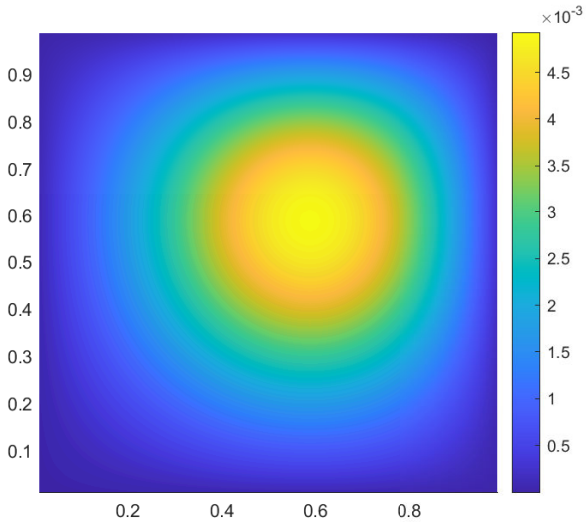

Figure 4: Concentration of chemical signal under diffusion at $t = 15\,\mathrm{h}$.

presents the distribution of the chemical signal at the final time level $t = 15\,\mathrm{h}$ and will serve as a reference for comparison in the simulations of the upcoming sections.

4.6 *Chemotaxis* effect coupled with fluid pressure

We now analyze *chemotaxis* coupled with fluid pressure, illustrating the effects of the fluid flow on the cell movement for two different source terms: $q_0 = 22\,\mathrm{h}^{-1}$ and $q_0 = 100\,\mathrm{h}^{-1}$. In both cases, we still expect *chemotaxis* to be the dominant mechanism guiding cell movement, resulting in a trajectory similar to that observed in the previous case. However, due to the influence of the velocity field, induced by the fluid pressure, a slight upward movement of the cells is anticipated, as illustrated by the velocity field in Figure 5.

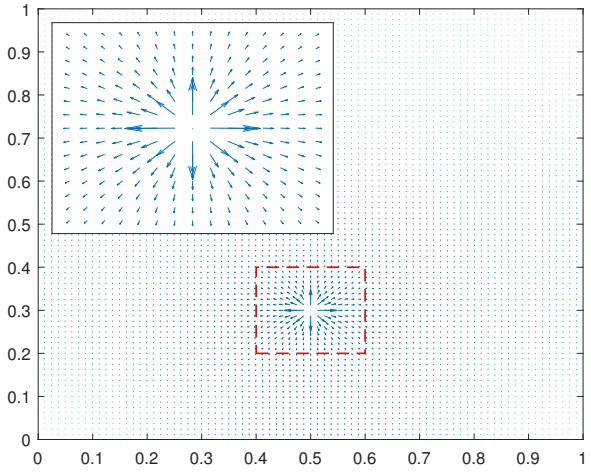

Figure 5: Velocity field under flow with $q_0 = 22\,\mathrm{h}^{-1}$. The top left plot is a zoom in on the dashed box.

As *chemotaxis* continues to be the dominant driving force, we plot only the final time level for both the cell density and chemical signal concentration. For comparison, Figure 6 presents the plots of cell and chemical signal distributions, for different fluid source terms, at $t = 15\,\mathrm{h}$. The influence of the fluid flow, increasing with the flow rate q_0, causes an upward displacement of both the cell density and the

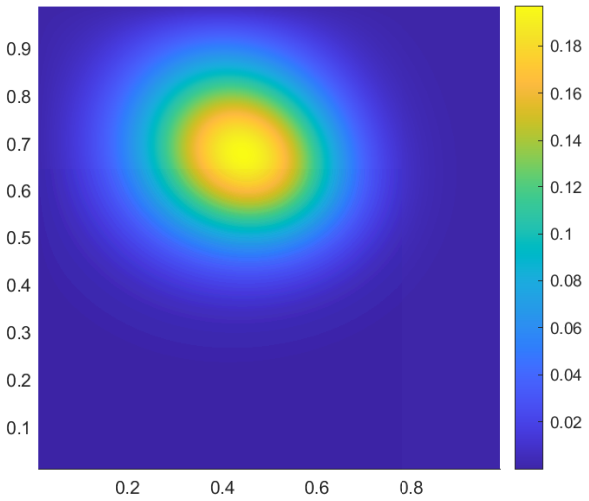

(a) Cell density, *chemotaxis* only

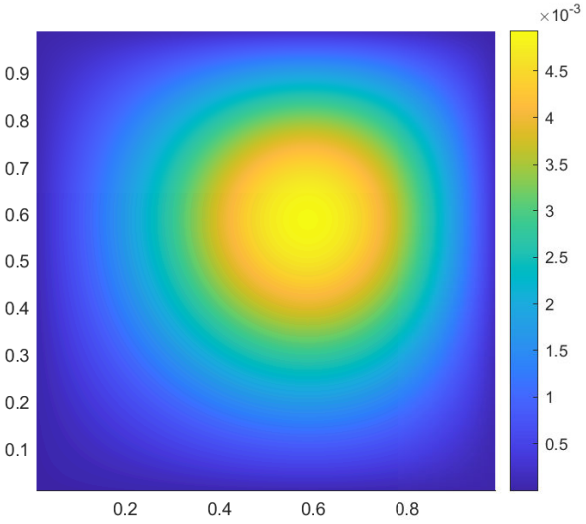

(b) Chemical concentration, *chemotaxis* only

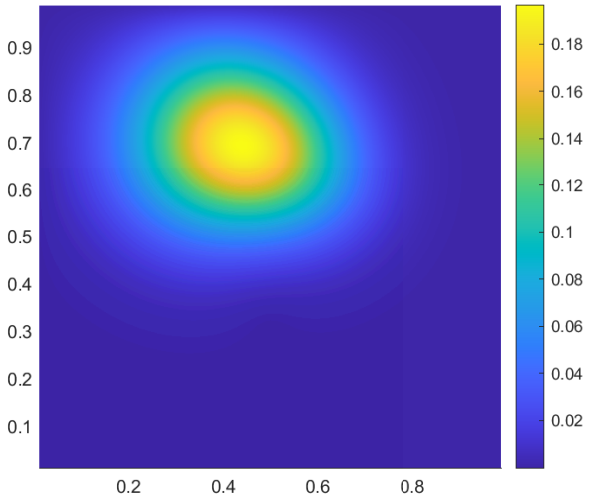

(c) Cell density, $q_0 = 22\,\mathrm{h}^{-1}$

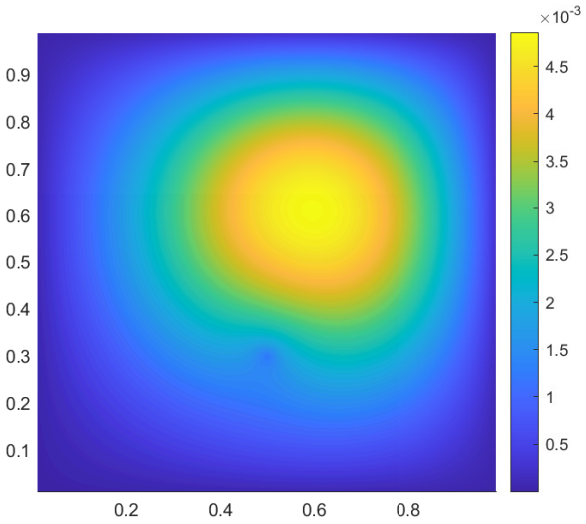

(d) Chemical concentration, $q_0 = 22\,\mathrm{h}^{-1}$

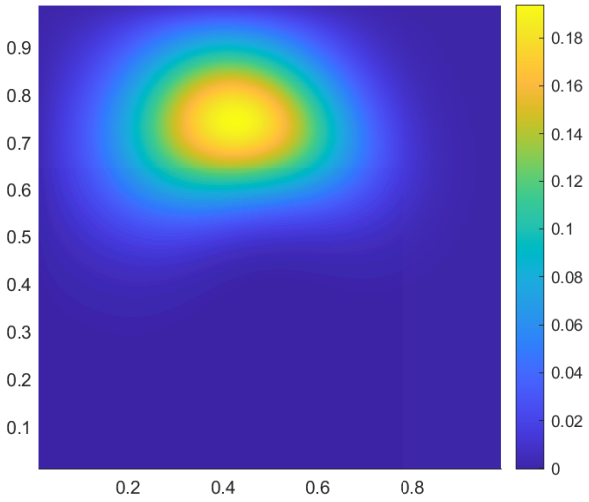

(e) Cell density, $q_0 = 100\,\mathrm{h}^{-1}$

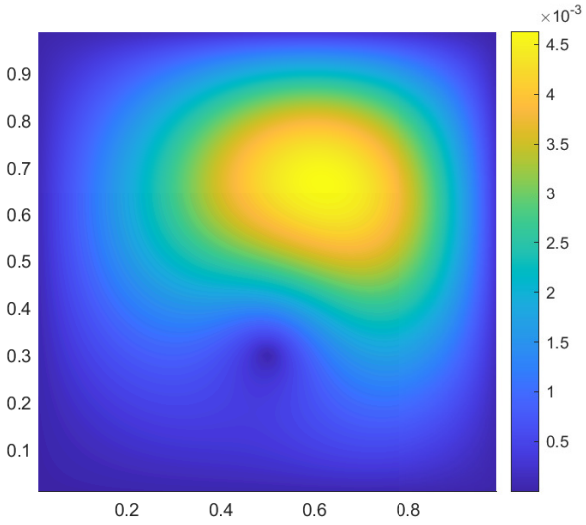

(f) Chemical concentration, $q_0 = 100\,\mathrm{h}^{-1}$

Figure 6: Simulation results at $t = 15\,\mathrm{h}$. Results are shown for: (a)-(b) *chemotaxis* only; (c)-(d) *chemotaxis* and flow with $q_0 = 22\,\mathrm{h}^{-1}$; and (e)-(f) *chemotaxis* and flow with $q_0 = 100\,\mathrm{h}^{-1}$.

chemical signal concentration, as globally depicted in Figure 6. Specifically, when we compare the no-flow scenario to the intermediate rate ($q_0 = 22\,\mathrm{h}^{-1}$) and the high rate ($q_0 = 100\,\mathrm{h}^{-1}$), the upward shift is clearly exhibited in the resulting cell density fields (Figures 6c and 6e) and the chemical concentration fields (Figures 6d and 6f). Furthermore, in both flow scenarios, a distinct region immediately adjacent to the fluid source is depleted of the chemical signal, with its concentration approaching zero.

We also plot the percentage of cancer cells that migrated to the chamber. Figure 7 illustrates three different scenarios: *chemotaxis* alone, *chemotaxis* combined with fluid flow for flow source term $q_0 = 22\,\mathrm{h}^{-1}$ and *chemotaxis* combined with fluid flow with $q_0 = 100\,\mathrm{h}^{-1}$. As expected, the scenario

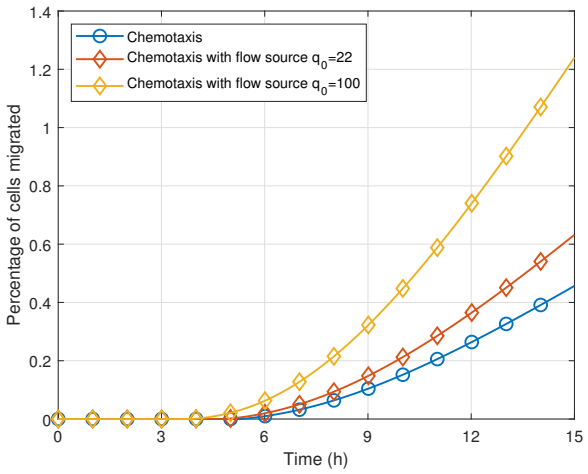

Figure 7: Percentage of cells migrated to the chamber under *chemotaxis*, *chemotaxis* plus fluid flow with $q_0 = 22\,\mathrm{h}^{-1}$ and *chemotaxis* plus fluid flow with $q_0 = 100\,\mathrm{h}^{-1}$.

with *chemotaxis* alone exhibits the lowest migration rate, reflecting the limited directional guidance provided solely by the chemical gradient. When fluid flow is introduced, the migration rate increases in both cases. A higher source term ($q_0 = 100\,\mathrm{h}^{-1}$) results in a greater percentage of migrated cells compared to $q_0 = 22\,\mathrm{h}^{-1}$, confirming that increased fluid mobility amplifies the influence of the pressure field on cell transport.

4.7 *Chemotaxis* effect coupled with fluid pressure and displacement

We now consider the fully coupled problem, where migration is influenced by *chemotaxis*, fluid velocity and tissue displacement. For this simulation, the fluid source parameter is set to $q_0 = 100\,\mathrm{h}^{-1}$ and the displacement field is given by a Gaussian profile centered in the domain with zero initial velocity, that is

$$u_i(x, y, 0) = \frac{1}{35}\, e^{-\frac{(x-0.5)^2+(y-0.5)^2}{0.04^2}} \quad \text{and} \quad \frac{\partial u_i}{\partial t}(x, y, 0) = 0,$$

for $i = 1, 2$, $(x, y) \in \Omega$ and we set $E_0 = 0.005$.

Figure 8 compares the percentage of cells that migrate to the chamber under three different scenarios: *chemotaxis*, *chemotaxis* combined with fluid flow and *chemotaxis* combined with both fluid flow and mechanical displacement in the tissue. Including displacement with flow ($q_0 = 100\,\mathrm{h}^{-1}$) leads to slightly higher cell migration compared to flow alone, as shown in Figure 8a. However, the difference is minimal, suggesting that displacement has a marginal effect in this regime, likely due to the dominant influence of fluid pressure. Consequently, we do not include additional visualizations for this scenario.

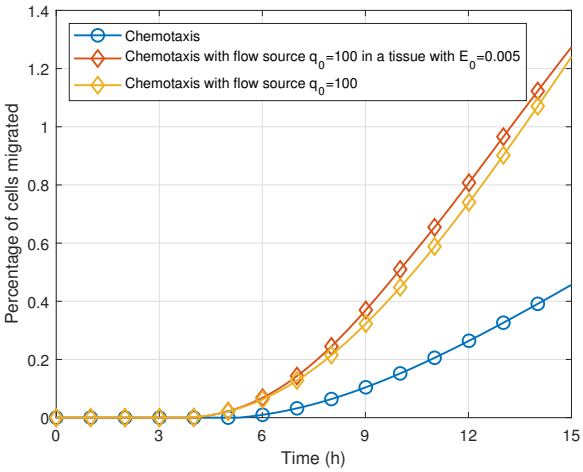

(a) Influence of displacement and fluid flow ($q_0 = 100\,\mathrm{h}^{-1}$).

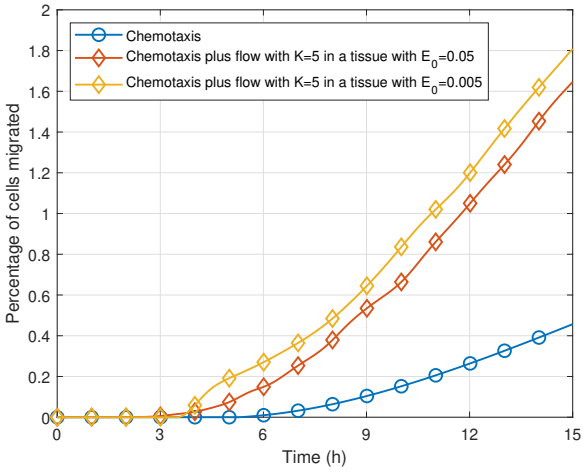

(b) Influence of stiffness (E_0), with $K = 5$ and $q_0 = 22\,\mathrm{h}^{-1}$.

Figure 8: Percentage of cells migrated to the chamber over time under various fluid flow and displacement conditions.

To further investigate the potential role of displacement, we take $q_0 = 22\,\mathrm{h}^{-1}$, $K = 5$ and consider two values for the Young modulus: $E_0 = 0.005$ and $E_0 = 0.05$. As illustrated in Figure 8b, the percentage of cells reaching the chamber begins increasing earlier than in the previously tested conditions. Additionally, the final percentages are higher for both cases. The initial stages of cell movement also display a more irregular behavior, possibly due to transient effects caused by the interplay between fluid flow and mechanical displacement. Another important observation steaming from Figure 8b is that the percentage of cells migrated to the chamber is consistently higher in the softer tissue. This suggests that, under the combined influence of *chemotaxis*, fluid pressure and displacement, cell migration is more effectively promoted in softer tissues.

4.8 *Chemotaxis* effect with fluid pressure and displacement with a source term

The final case of interest concerns the continuous emission of mechanical waves, aimed at investigating the impact of sustained mechanical stimulation on migration. In this scenario, we assume no initial displacement or velocity in the tissue. Instead, wave generation is modeled through a time-dependent source term in the displacement equation, given by:

$$f(x,y,t) = A\exp\left(-\frac{(x-0.5)^2}{2\sigma_x^2} - \frac{(y-0.5)^2}{2\sigma_y^2}\right)\sin(\omega t), (x,y) \in \Omega,\ t \in (0,T),$$

where A is the amplitude, σ_x and σ_y are the standard deviations and ω is the angular frequency. This term continuously emits waves centered at $(0.5, 0.5)$. We consider the parameters $A = 0.1$, $\sigma_x = \sigma_y = 0.02$ and angular frequencies $\omega = 200\pi$ and $\omega = 100\pi$. All other parameters remain as specified in Table 1. Our objective is to analyze the effect of this *stimulus* on migration in two tissues with different stiffness profiles: $E_0 = 5 \times 10^{-4}$ and $E_0 = 5 \times 10^{-5}$. Figure 9b shows the percentage of cells that migrate to the chamber under *chemotaxis* and *chemotaxis* combined with fluid flow with $q_0 = 22\,\mathrm{h}^{-1}$, $\omega = 200\pi$.

Recalling that the percentage of cells migrated under *chemotaxis* combined with fluid flow ($q_0 =$

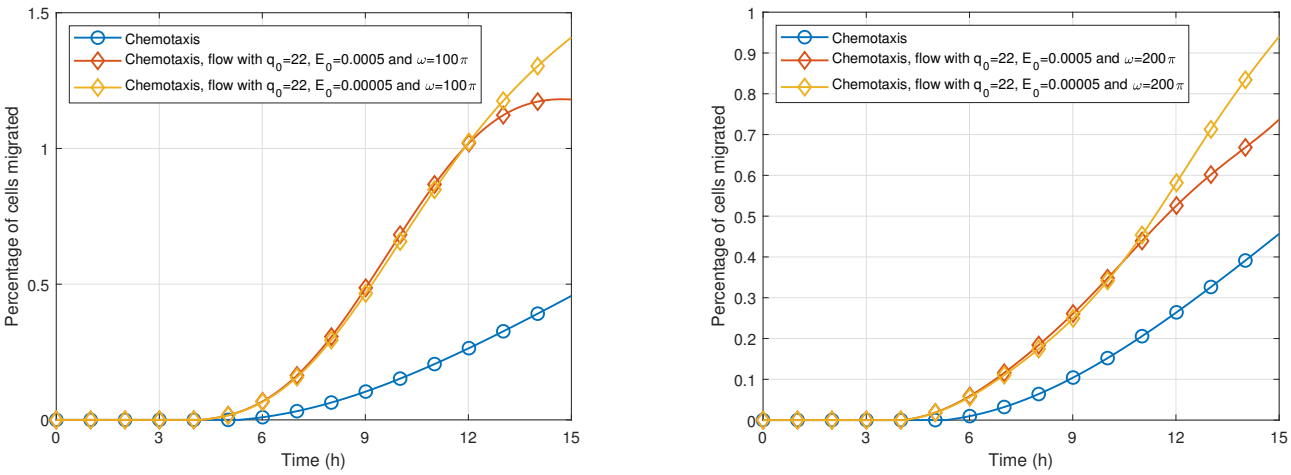

(a) $\omega = 100\pi$. (b) $\omega = 200\pi$.

Figure 9: Percentage of cells migrated over time under sustained mechanical wave stimulation (with $q_0 = 22\,\mathrm{h}^{-1}$), comparing two angular frequencies across tissues with different stiffnesses.

$22h^{-1}$) was approximately 0.6% (see Figure 7), we observe that the addition of wave stimulation results in a higher migration rate. This suggests that the combined influence of fluid pressure and sustained mechanical waves significantly enhances cell motility. Furthermore, we note that the stiffer tissue ($E_0 = 5 \times 10^{-4}$) leads to reduced migration compared to the softer case ($E_0 = 5 \times 10^{-5}$). Interestingly, both migration curves remain nearly identical until approximately $t = 11\,\mathrm{h}$, after which differences begin to emerge.

We also reduced the angular frequency to $\omega = 100\pi$ while keeping all other parameters unchanged, to assess its influence. As shown in Figure 9a, this reduction further increases cell migration. In the stiffer tissue, the percentage of migrated cells rises to approximately 1.2%, while in the softer tissue this value reaches about 1.4%. These values represent a noticeable increase compared to the 0.73% and 0.93% observed in the higher frequency case, respectively. This suggests that lower frequency mechanical stimulation promotes greater cellular movement. Additionally, both curves remain similar up to $t = 12\,\mathrm{h}$, after which the stiffer tissue again shows a slower increase in migration, consistent with the behavior observed under higher frequency conditions.

5 Conclusions

This paper presented a numerical method for the nonlinear system of partial differential equations (1)-(4) that combines two convection-diffusion-reactions equations and an elliptic and a wave-type equation. The convective transport in the two first equations depends on the gradient of the solution of the elliptic equation and the time derivative of the solution of the wave equation.

It should be pointed out that (1)-(4) can be considered to describe cancer cell migration when *chemotaxis*, fluid pressure and mechanical displacement of the tissue are the relevant phenomena in cell migration. This model extended previous work in [11] by including tissue displacement through a linear elastic model (Hooke's law). A semidiscrete finite difference scheme was proposed and analyzed, establishing second-order of convergence in space for all variables of the system, under suitable smoothness assumptions and second-order initial data approximation. Numerical simulations with an

IMEX method based on the semidiscrete scheme confirmed the theoretical convergence rates. The nonlinearity nature of the problem as well as the dependence of the convective transport on the solution of the elliptic and wave equations and the presence of mixed derivatives in the wave equation pose intricate mathematical challenges that were addressed in the present work.

Numerical simulations allow us to draw some insights regarding the interplay between *chemotaxis*, fluid pressure and displacement on cancer cell migration. In high-flow regimes ($q_0 = 100\,\mathrm{h}^{-1}$), fluid pressure dominates over mechanical displacement. However, when fluid flow is reduced ($q_0 = 22\,\mathrm{h}^{-1}$), mechanical displacement plays a more important role. On our analysis, softer tissues show higher migration rates compared to stiffer tissues. We also concluded that sustained mechanical waves, modeled through a time-dependent source term, significantly enhanced migration compared to all other cases.

Acknowledgments

The authors acknowledge financial support by the Centre for Mathematics of the University of Coimbra (CMUC, https://doi.org/10.54499/UID/00324/2025) under the Portuguese Foundation for Science and Technology (FCT), Grants UID/00324/2025 and UID/PRR/00324/2025. Augusto Fernandes was also supported by the FCT PhD grant PD/BD/152073/2021, funded by the Portuguese Government through FCT/MCTES.

References

[1] G. Arumugam and J. Tyagi. Keller-Segel Chemotaxis Models: A Review. *Acta Applicandae Mathematicae*, 171(1):6, 2020.

[2] N. Bellomo, A. Bellouquid, Y. Tao, and M. Winkler. Toward a mathematical theory of Keller–Segel models of pattern formation in biological tissues. *Math. Models Methods Appl. Sci.*, 25(9):1663–1763, 8 2015.

[3] J. Bonilla and J. Vicente Gutiérrez-Santacreu. Exploring numerical blow-up phenomena for the Keller-Segel-Navier-Stokes equations. *Journal of Numerical Mathematics*, 32(2), 2023.

[4] M. Chae, K. Kang, and J. Lee. Existence of smooth solutions to coupled chemotaxis-fluid equations. *Discrete and Continuous Dynamical Systems*, 33(6):2271–2297, 2013.

[5] A. Chertock, K. Fellner, A. Kurganov, A. Lorz, and P. A. Markowich. Sinking, merging and stationary plumes in a coupled chemotaxis-fluid model: a high-resolution numerical approach. *Journal of Fluid Mechanics*, 694:155–190, 2012.

[6] A. Chertock and A. Kurganov. A second-order positivity preserving central-upwind scheme for chemotaxis and haptotaxis models. *Numer. Math.*, 111(2):169–205, 11 2008.

[7] Y. Deleuze, C.-Y. Chiang, M. Thiriet, and T. W. Sheu. Numerical study of plume patterns in a chemotaxis-diffusion-convection coupling system. *Computers & Fluids*, 126:58–70, 2016.

[8] R. Duan, A. Lorz, and P. Markowich. Global Solutions to the Coupled Chemotaxis-Fluid Equations. *Communications in Partial Differential Equations*, 35(9):1635–1673, 2010.

[9] A. Duarte-Rodríguez, M. Á. Rodríguez-Bellido, D. A. Rueda-Gómez, and É. J. Villamizar-Roa. Numerical analysis for a chemotaxis-Navier-Stokes system. *ESAIM: Mathematical Modelling and Numerical Analysis*, 55:S417–S445, 2021.

[10] Y. Epshteyn and A. Kurganov. New Interior Penalty Discontinuous Galerkin Methods for the Keller–Segel Chemotaxis Model. *SIAM Journal on Numerical Analysis*, 47(1):386–408, 2009.

[11] A. Fernandes, J. A. Ferreira, and L. Pinto. Numerical analysis of a Keller-Segel-Flow model for tumor cell migration. *Mathematics and Computers in Simulation*, 238:65–81, 2025.

[12] J. Ferreira, L. Pinto, and R. Santos. Numerical analysis of a porous-elastic model for convection enhanced drug delivery. *Computers and Mathematics with Applications*, 107:113719, Jan. 2022.

[13] J. A. Ferreira and R. D. Grigorieff. Supraconvergence and supercloseness of a scheme for elliptic equations on nonuniform grids. *Numerical Functional Analysis and Optimization*, 27(5-6):539–564, 2006.

[14] T. Hillen and K. J. Painter. A user's guide to PDE models for chemotaxis. *Journal of Mathematical Biology*, 58(1):183–217, 2009.

[15] Z. Hu. Suppression of Chemotactic Singularity via Viscous Flow with Large Buoyancy. *SIAM Journal on Mathematical Analysis*, 56(6):7866–7902, 2024.

[16] X. Huang and J. Shen. Bound/positivity preserving sav schemes for the Patlak-Keller-Segel-Navier-Stokes system. *Journal of Computational Physics*, 480:112034, 2023.

[17] C. Ji and Y. Huang. Durotaxis and negative durotaxis: where should cells go? *Communications Biology*, 6, 11 2023.

[18] E. F. Keller and L. A. Segel. Initiation of slime mold aggregation viewed as an instability. *Journal of Theoretical Biology*, 26(3):399–415, 1970.

[19] E. F. Keller and L. A. Segel. Model for chemotaxis. *Journal of Theoretical Biology*, 30(2):225–234, 1971.

[20] I. Lampropoulos and M. Kavousanakis. Application of combination chemotherapy in two dimensional tumor growth model with heterogeneous vasculature. *Chemical Engineering Science*, 280:118965, 2023.

[21] H. G. Lee and J. Kim. Numerical investigation of falling bacterial plumes caused by bioconvection in a three-dimensional chamber. *European Journal of Mechanics - B/Fluids*, 52:120–130, 2015.

[22] C.-M. Lo, H.-B. Wang, M. Dembo, and Y.-l. Wang. Cell Movement Is Guided by the Rigidity of the Substrate. *Biophysical Journal*, 79(1):144–152, 2000.

[23] A. Lorz. A coupled Keller–Segel–Stokes model: global existence for small initial data and blow-up delay. *Commun. Math. Sci.*, 10(2):555–574, 2012.

[24] C. Phipps and M. Kohandel. Mathematical model of the effect of interstitial fluid pressure on angiogenic behavior in solid tumors. *Comput. Math. Methods Med.*, 2011(1):843765, 9 2011.

[25] W. J. Polacheck, J. L. Charest, and R. D. Kamm. Interstitial flow influences direction of tumor cell migration through competing mechanisms. *Proceedings of the National Academy of Sciences*, 108(27):11115–11120, 2011.

[26] G. S. Rosalem, E. B. Las Casas, T. P. Lima, and L. A. González-Torres. A mechanobiological model to study upstream cell migration guided by tensotaxis. *Biomechanics and Modeling in Mechanobiology*, 19(5):1537–1549, 2020.

[27] A. Shellard and R. Mayor. Durotaxis: The Hard Path from *in vitro* to *in vivo*. *Developmental Cell*, 56(2):227–239, 2021.

[28] J. Shen and J. Xu. Unconditionally Bound Preserving and Energy Dissipative Schemes for a Class of Keller–Segel Equations. *SIAM Journal on Numerical Analysis*, 58(3):1674–1695, 2020.

[29] J. D. Shields, M. E. Fleury, C. Yong, A. A. Tomei, G. J. Randolph, and M. A. Swartz. Autologous Chemotaxis as a Mechanism of Tumor Cell Homing to Lymphatics via Interstitial Flow and Autocrine CCR7 Signaling. *Cancer Cell*, 11(6):526–538, 2007.

[30] K. Stoverund, M. Darcis, R. Helmig, and S. M. Hassanizadeh. Modeling concentration distribution and deformation during convection-enhanced drug delivery into brain tissue. *Transport in Porous Media*, 92(1):45, 2012.

[31] T. Stylianopoulos, J. D. Martin, M. Snuderl, F. Mpekris, S. R. Jain, and R. K. Jain. Coevolution of Solid Stress and Interstitial Fluid Pressure in Tumors During Progression: Implications for Vascular Collapse. *Cancer Research*, 73(13):3833–3841, 6 2013.

[32] Y. Tang, G.-a. Zou, and J. Li. Unconditionally energy-stable finite element scheme for the chemotaxis-fluid system. *Journal of Scientific Computing*, 95(1), 2023.

[33] Y. Tao and M. Winkler. Global existence and boundedness in a Keller-Segel-Stokes model with arbitrary porous medium diffusion. *Discrete and Continuous Dynamical Systems*, 32(5):1901–1914, 2012.

[34] C. Villa, M. A. J. Chaplain, A. Gerisch, and T. Lorenzi. Mechanical models of pattern and form in biological tissues: the role of stress-strain constitutive equations. *Bulletin of Mathematical Biology*, 83(80), 2021.

[35] J. O. Waldeland, J.-V. Gaustad, E. K. Rofstad, and S. Evje. In silico investigations of intratumoral heterogeneous interstitial fluid pressure. *Journal of Theoretical Biology*, 526:110787, 2021.

[36] M. Wang, G.-a. Zou, B. Wang, and W. Zhao. Unconditionally energy-stable discontinuous galerkin method for the chemo-repulsion-Navier-Stokes system. *Computers & Mathematics with Applications*, 150:132–155, 2023.

[37] M. R. Zanotelli and C. A. Reinhart-King. Mechanical Forces in Tumor Angiogenesis. *Advances in experimental medicine and biology*, 1092:91–112, 2018.

[38] L. Zhang, Y. Ge, and X. Yang. High-accuracy positivity-preserving numerical method for Keller-Segel model. *Math. Biosci. Eng.*, 20(5):8601–8631, 3 2023.